



UNIVERSITÁ DEGLI STUDI DI MILANO
Facoltà di Scienze Matematiche Fisiche e Naturali
Corso di Laurea Magistrale in Fisica

**Small x resummed evolution equations and their
implementation in a parton fit**

Relatore: Prof. Stefano Forte

Correlatore: Dott. Juan Rojo

**Tesi di laurea di:
Maria Giulia CALZOLAIO
Matr. 737676
Codice P.A.C.S.: 12.38.-t**

Anno Accademico 2009-2010

Contents

Introduction	5
1 Quantum Chromodynamics	11
1.1 Foundations of QCD	11
1.1.1 The experimental evidence for <i>Colour</i>	11
1.1.2 Asymptotic freedom	12
1.2 QCD beyond leading order	16
1.2.1 The factorization theorem in DIS	16
1.2.2 DGLAP equation	20
2 Small x Resummation	27
2.1 Small x evolution equations	27
2.1.1 Small x anomalous dimensions	28
2.1.2 The path-integral method to solve DGLAP equation	31
2.2 ABF approach to small x resummation	33
2.2.1 The three ingredients for stable small x resummation	33
2.2.2 Phenomenological results	38
3 NNPDF approach to the parton fit	43
3.1 Experimental data and Monte Carlo generation	44
3.2 Fitting strategy with neural networks	48
3.3 FastKernel method	49
3.3.1 Fast PDF evolution	50
3.3.2 Fast computation of DIS observables	51
3.4 Results	52
4 Implementation of small x resummation in the NNPDF code	57
4.1 Preliminary studies	57
4.1.1 Splitting functions	60
4.1.2 Coefficient functions	62
4.2 Implementation of small x resummation in the FastKernel code	65

4.2.1	Structure of FastKernel code	65
4.2.2	Logics of the Fortran implementation	67
4.2.3	Checks and results	69
4.3	Future works	70

Introduction

”There are therefore Agents in Nature able to make the Particles of Bodies stick together by very strong Attractions. And it is Business of experimental Philosophy to find them out”

Isaac Newton, *Optics*

The aim of particle physics is finding the fundamental constituents of matter and understanding how they interact with one another. The present work has exactly this spirit. In fact, my purpose is try to understand more deeply the structure of a nucleon. To realize this goal what is needed is a deep understanding of the experimental datas nowadays available about the nucleon, through an accurate knowledge of the Quantum Chromodynamics (QCD), that is the theory of strong interactions.

The internal structure of a composite system (such as atoms, nuclei or nucleons) can be probed through scattering. We can perform fixed target experiments, with an accelerated beam of light particle colliding with a fixed target, or colliders, with two particle beams accelerated against each other. To investigate the structure of particles, the simplest way is bombarding it with a particle beam and studying the final angular distribution of the projectiles. Depending on the energy available in the center of mass system, we can ”see” the particle in its whole structure (that is spatial extension, charge distribution and so on) or we can probe directly its constituents, through the excitation of resonant states or even breaking the particles of the target. In fact, this was the way that brought the physicists of last century to discover the composite structure of the atomic nucleus, as made of neutrons and protons.

When they turned to the constituents of the nucleus, the first evidence was the similarity between them: proton and neutron have same spin-parity $J^P = \frac{1}{2}^+$, almost the same mass ($\frac{m_n - m_p}{m_p} \approx 1.4 \cdot 10^{-3}$) and they differ only in charge. Physicists started to think of them as two different states, degenerate in energy, of the same particle, the nucleon. From a theoretical point of view, this means that $|p\rangle$ and

$|n\rangle$ can be seen as basis vectors of a bidimensional Hilbert space and that the Hamiltonian of the new interaction should be invariant under $p \leftrightarrow n$ exchange, that is under the isospin $SU(2)_f$ group.

Then something strange happened: the experimental evidence was that the nucleons had an internal structure, but experiments always failed to observe their constituents (called partons) as free particles. The way this came about is the following. Increasing the energy of the colliding beam, a lot of new heavy particles, called hadrons, were seen and the introduction of new quantum numbers (e.g. *strangeness*) became necessary. Therefore, the isospin symmetry, postulated before, was not enough to explain this particles proliferation. Theoretical physicists tried different ways to extend the $SU(2)_f$ symmetry to $SU(3)_f$. Sakata proposed that strong interactions should be invariant under exchange between proton, neutron and the strange particle Λ^0 ; this symmetry, though, was not exact, because the mass difference between proton and Λ^0 is approximately of 19% and brought to more baryon states than are physically observed. Gell-Mann gave the idea of the so-called "Eight fold way": baryons, that is hadrons with proposed half-integer spin, can be assigned to multiplets (octet and decuplets), depending on their spin-parity J^P ; these multiplets can be obtained from the fundamental representation of $SU(3)$ as :

$$3 \otimes 3 \otimes 3 = 10 \oplus 8 \oplus 8 \oplus 1 \quad (1)$$

The "Eight fold way" was confirmed by the discovery of the Ω^0 particle, but its main problem remained open: does the fundamental representation correspond to any real physical state? The answer to this question came with deep inelastic scattering (DIS) experiments. In Figure 1 a diagrammatic representation of the

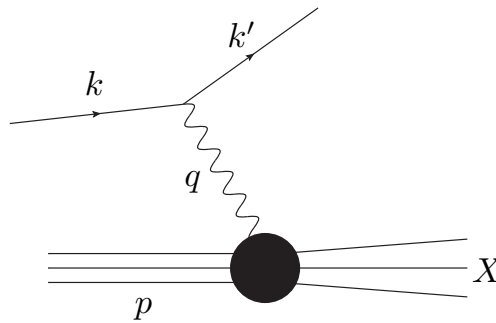


Figure 1: The Deep Inelastic process

scattering between an electron and a nucleon is shown. The kinematic variables for such a process are:

$$Q^2 = -q^2 \quad \nu = \frac{p \cdot q}{M} \quad x = \frac{Q^2}{2M\nu} \quad y = \frac{p \cdot q}{p \cdot k}. \quad (2)$$

DIS is characterized by the fact that the virtual photon interacts with a nucleon's constituent and it is the kinematic regime

$$Q^2, \nu \rightarrow \infty \text{ and } x \text{ finite.} \quad (3)$$

The results of DIS experiments showed that the structure functions of the nucleon obey an approximate *scaling* law, namely they do not depend on Q^2 . The physical interpretation of this behavior was that the nucleon's constituents are pointlike, carry a fraction of nucleon total momentum and are almost free. The fact that scaling was not exact is also very important, because it was not yet understood how the partons interact with one another and interaction gives a structure also at elementary particles (as for the electron).

After all these studies physicists started to believe that the states in the fundamental representation are real physical particles, called *quarks*, with fractional electric charge ($\pm\frac{1}{3}, \pm\frac{2}{3}$), baryon number equal to $\frac{1}{3}$ and spin $\frac{1}{2}$. It was the birth of parton model. Despite all this progress, a lot of unsolved questions still remained, such as: why do quarks behave as free particles in DIS, but in fact can not be seen as free particles? Why is the scaling not exact? Quantum Chromodynamics, namely the theory of strong interactions, explains these issues.

As I will describe in more detail in Chapter 1, in QCD the analogue of the electric charge is not flavour, but rather a new degree of freedom called *colour*. In nature free particles with non zero colour cannot exist. Partons do carry colour and this is the reason why it is impossible to see them as free particles. This phenomenon is called *confinement* and it is related to another crucial aspect of the strong interactions: *asymptotic freedom*. This means that, in the perturbative regime, the strong coupling is large at large distances, but it is predicted to be small at short distances so that partons behave as free particles at asymptotically high energies, justifying the use of perturbation theory to perform process calculations.

So, we know that partons build up the nucleon and we also know that with our calculation we can not predict perturbatively the actual distributions of the parton in the nucleon (due to strong coupling), but is there an indirect way to see *how* they actually form the nucleon? From experimental data can we get any information about the distributions of partons inside the nucleon?

The *collinear factorization theorem* in equation (4) is a classical result of QCD

and can help answering these questions:

$$\sigma_{tot}(x, Q^2) = \sum_{i=1}^{n_f} \int_{x_{min}}^1 \frac{dy}{y} \hat{\sigma}_i\left(\frac{x}{y}, \alpha_s(Q^2)\right) f_i(y, Q^2) = \sum_{i=1}^{n_f} \hat{\sigma}_i \otimes f_i(x, Q^2) \quad (4)$$

It allows us to calculate hadronic cross-sections in terms of a convolution of a partonic perturbatively computable cross-section, with non-perturbative but process-independent functions, called parton distribution functions (PDFs).

Although PDFs are non-perturbative, their evolution with respect to the energy scale of the process is given by DGLAP evolution equation ¹:

$$\mu^2 \frac{\partial}{\partial \mu^2} f_i(x, \mu^2) = \frac{\alpha_s(\mu^2)}{2\pi} P_{ij}(x, \alpha_s(\mu^2)) f_j(x, \mu^2), \quad (5)$$

where $P_{ij}(x, \alpha_s(\mu^2))$ are called *splitting function*. From equation (5) we see that, given the PDFs at some initial scale, we can find them at any other scale, provided both scales are large enough that the coupling is in the perturbative regime. Other details will be given in the next chapter; what is important to underline here is that through the knowledge of PDFs we can get information on how the partons build up the nucleon and, thus using equation (4), predict the expected total cross-sections.

It is clear from equation (4) that to have information about PDFs from data we need to perform a calculation as accurate as possible of partonic cross sections and of the splitting functions, which determine PDFs' evolution with the scale.

At present, we can perform the calculation of QCD quantities at NLO and often also at NNLO. Nevertheless when we have to deal with data coming from high-energy colliders (such as LHC) we may need a more accurate level of approximation. In fact, at high-energy colliders, the contribution of small x QCD becomes important.

For small x regime of QCD we mean the regime where a scattering process is governed by two different large scales, namely the center of mass energy of the colliding beams S and the hard scale Q^2 (which for typical hadron collider processes is related to a final-state scale). The x parameter measures the ratio between the two scales:

$$x = \frac{Q^2}{S} \quad (6)$$

The presence of different large scales implies that several large scales ratios can be formed. Indeed, observables computed in perturbation theory contain terms

¹The equation (5) is valid only for "non-singlet" parton distributions: $q_{NS} = q_i - q_j$

$\alpha_s \log(\frac{1}{x})$, that can become of order 1 when $x \rightarrow 0$, spoiling the perturbative expansion. Partonic cross sections are then poorly behaved at small x and PDFs, obtained by fitting data with them, are unstable. This bad small x behaviour of both PDFs and partonic cross sections turns into an uncertainty of total hadronic cross-sections, which can be a problem for future precision physics at the Large Hadron Collider. Indeed, LHC push the small x regime down to $x \sim 10^{-6} - 10^{-7}$, two orders of magnitude below than at HERA, as shown in Figure 2. From

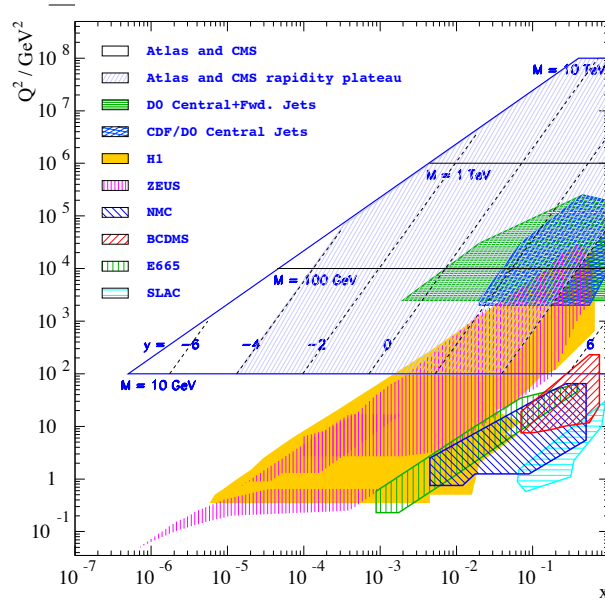


Figure 2: LHC kinematic range compared with older machines

all the previous considerations, the importance of small x resummation is plain. As I will explain in Chapter 2, the actual state of art is that a lot of processes have been resummed at LL x accuracy and also the PDFs evolution kernels have been computed [1], but these results have never been used to perform a global parton fit and find a set of small x resummed PDFs. The aim of this work is the implementation of resummed results in a parton fit. There are many different ways to carry out global PDFs fit. In this work I followed the NNPDF approach [2], which, as I will detail in Chapter 4, combines a Monte Carlo representation of the probability measure in the space of PDFs with the use of neural networks as a set of unbiased basis functions.

Chapter 1

Quantum Chromodynamics

Quantum Chromodynamics is the theory of the strong interaction, one of the four fundamental forces in nature. It describes the interactions between quarks and gluons, and in particular how they bind together to form hadrons. In this chapter I will introduce the fundamental aspects of QCD, from its foundations (section 1.1) to its theoretical properties beyond leading order (section 1.2).

1.1 Foundations of QCD

1.1.1 The experimental evidence for *Colour*

The first intimation of a new, unrevealed degree of freedom of matter came from baryon spectroscopy. For a baryon made of three spin- $\frac{1}{2}$ quarks, the parton model wavefunction takes the form:

$$\Psi_{3q} = \Psi_{space} \cdot \Psi_{spin} \cdot \Psi_{flavour} \quad (1.1)$$

This wavefunction is *symmetric* under exchange of any two quarks, violating the Pauli exclusion principle that requires fermions to have an *antisymmetric* wavefunction. A simple way to solve this problem is to assume that the quarks carry a new degree of freedom, called *colour*, with respect to which the Ψ_{3q} in (1.1) can be antisymmetrised. Then, one can introduce a wavefunction Ψ^a , where the "colour" index a can assume three values, corresponding to the three possible state of colour (red, blue and green). With the addition of this degree of freedom we can form a three-quark wavefunction which is antisymmetric in colour:

$$\Psi_{3q}^{colour} = \epsilon_{abc} \Psi^a \Psi^b \Psi^c \quad (1.2)$$

A very important observation is that equation (1.2) besides being antisymmetric it is invariant upon $SU(3)_c$ transformations, i.e. it is a colour *singlet*.

The verification of the hypothesis of colour comes from observations. In fact, if the quarks can be found in three different states of colour, the increase in the number of quark types must be seen in measured QED cross sections. For example, at high energies, the ratio

$$R = \frac{\sigma(e^+ e^- \rightarrow \text{hadrons})}{\sigma(e^+ e^- \rightarrow \mu^+ \mu^-)} \quad (1.3)$$

at leading order is simply equal to the sum of possible $q\bar{q}$ final states, each weighted by the square of its electric charge:

$$R = \sum_a e_a^2 \quad (1.4)$$

where the index a runs over all quark types. If we consider five active flavours u, d, s, c, b with respective charges $\frac{2}{3}, -\frac{1}{3}, -\frac{1}{3}, \frac{2}{3}, -\frac{1}{3}$, we get for $R = \frac{11}{9}$ without color, but $R = \frac{11}{3}$ with color. At energies above the b threshold are in reasonable agreement with $R_{\text{colour}} = \frac{11}{3}$.

Another process in which the color factor is relevant is Dell-Yan, which, in the parton model, involves the subprocess:

$$q\bar{q} \rightarrow l\bar{l} \quad (1.5)$$

To get the correct cross-section it is necessary to provide a factor of $\frac{1}{3}$, obtained by the averaging over the nine possible initial $q\bar{q}$ combinations and then summing over the number of such states that lead to the colour neutral photon, which is 3 ($r\bar{r}$, $b\bar{b}$, $g\bar{g}$). Even adding such a factor, though, the leading order total cross section is still about half of the measured value. This discrepancy is due to higher order corrections and it means that the free parton model is not enough. A dynamics of colour (QCD) is needed to fully understand quark's behaviour.

1.1.2 Asymptotic freedom

From a theoretical point of view, QCD is a non abelian gauge theory, with symmetry group $SU(3)_c$. The subscript c is to underline that the gauge group is color $SU(3)$, not to be confused with flavour $SU(3)$. The quanta of the $SU(3)$ gauge field are called *gluons* and, differently from the photon in QED, they carry colour. The non abelian nature of $SU(3)$ is the origin of the colored gluon.

The perturbative calculation of any process requires the use of Feynman rules that can be derived from the Lagrangian density of the interaction. The expression for QCD Lagrangian density is shown in equation (1.6), where g_s is the dimensionless intensity of the strong coupling, A_μ^a is the gluon field (note the colour index a),

the λ_a are the eight generators of SU(3) [7]. In equation (1.7) the expression of the field strength tensor is also shown, where f_{abc} are the structure constants of SU(3) group.

$$\mathcal{L}_{QCD} = \sum_{flavours} [\bar{\Psi}_f (i\partial - m_f) \Psi_f + g_s A_\mu^a \bar{\Psi}_f \gamma^\mu \lambda_a \Psi_f] - \frac{1}{4} F_{\alpha\beta}^a F_a^{\alpha\beta} \quad (1.6)$$

$$F_{\alpha\beta}^a = (\partial_\mu A_\nu^a - \partial_\nu A_\mu^a + g_s f_{abc} A_\mu^b A_\nu^c) \quad (1.7)$$

At the quantum level, gauge-fixing and ghost contributions must be added to the Lagrangian (1.6). For details see [7].

The first thing to notice is that, in the field strength tensor in equation (1.7), there is a non Abelian term (the one proportional to g_s), which gives rise to cubic and quartic gluon self-interaction. This is a crucial property of QCD. In fact it is the origin of both asymptotic freedom and non gauge invariance of $F_{\alpha\beta}^a$. A detailed discussion of the latter can be found in [7]. In this section I will focus on asymptotic freedom.

A very important property of a renormalizable field theory is the running of the coupling constant: the strength of the coupling depends on the typical scale of the process we are studying. This running is governed by the renormalization group equation, which for $\alpha_s = \frac{g_s}{4\pi}$ has the form:

$$Q^2 \frac{\partial \alpha_s}{\partial Q^2} = \beta(\alpha_s). \quad (1.8)$$

The β function can be expanded in powers of α_s

$$\beta(\alpha_s) = -b\alpha_s^2(1 + b'\alpha_s + b''\alpha_s^2 + O(\alpha_s^3)), \quad (1.9)$$

where the expansion coefficients can be determined through a perturbative computation. Defining the renormalization scale μ^2 the first order solution for α_s to equation (1.8) is:

$$\alpha_s(Q^2) = \frac{\alpha_s(\mu^2)}{1 + \alpha_s(\mu^2)b \ln\left(\frac{Q^2}{\mu^2}\right)}. \quad (1.10)$$

This result is reliable in the perturbative region, where $\alpha_s(\mu^2), \alpha_s(Q^2) \ll 1$.

The calculation of the β function in QCD includes in addition to fermion loops in Figure 1.1, also the non Abelian diagrams in Figure 1.2. The inclusion of such diagrams with gluon loops leads to a β function different from the QED one. The

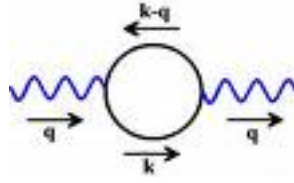


Figure 1.1: Diagram with one virtual loop of fermions

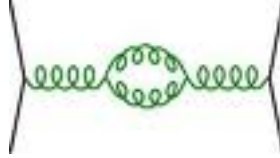


Figure 1.2: Diagram with one virtual loop of gluons

crucial difference is in the sign of the b coefficient, which determines the dependence of the coupling on Q^2 , as shown in equation (1.10). In fact:

$$b_{QCD} = \frac{33 - 2n_f}{12\pi} > 0 \text{ for } n_f \leq 16, \quad (1.11)$$

while $b_{QED} = -\frac{1}{6\pi} < 0$. The function $\alpha_s(Q^2)$ obtained using (1.11) in (1.10) has the announced asymptotically free behavior: as Q^2 becomes very large, $\alpha_s(Q^2)$ decreases to zero. Thus in QCD, the vacuum polarization, including also the production of spin-1 gluons, produces a sort of paramagnetic effect and increases the colour charge, so that, a decrease in the distance from the source implies a drop in the strength of the coupling. In Figure 1.3 the running of α_s is shown, compared with the running of α_{weak} and of α_{QED} .

It is useful to introduce Λ_{QCD}^2 , namely the scale at which α_s would diverge if extrapolated outside the perturbative domain. Qualitatively one can say that it indicates the order of magnitude of the scale at which $\alpha_s(Q^2)$ becomes strong. The condition that Λ_{QCD}^2 must satisfy is

$$\alpha_s(\Lambda_{QCD}^2) = +\infty, \quad (1.12)$$

which means, using equation (1.10),

$$1 + b_0 \alpha_s(\mu^2) \ln \left(\frac{\Lambda_{QCD}^2}{\mu^2} \right) = 0. \quad (1.13)$$

The value of Λ_{QCD}^2 is about 200 MeV. Thus $\alpha_s(Q^2)$ becomes large, and a perturbative approach to QCD is no more consistent, for scales comparable with the

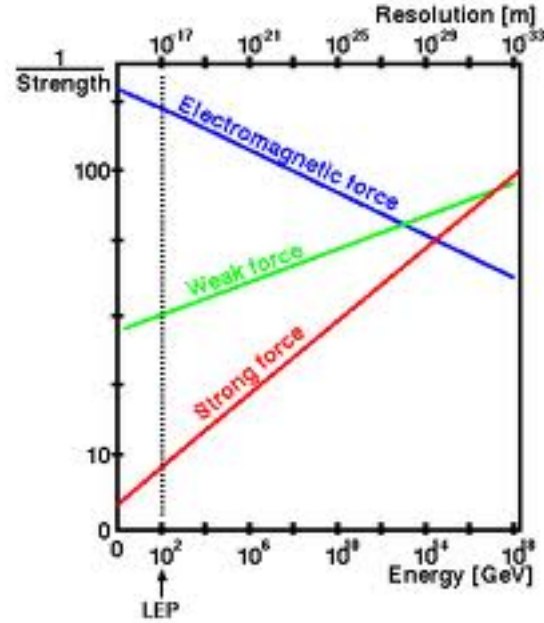


Figure 1.3: Running of α_s (red line), α_{weak} (green line) and α_{QED} (blue line)

masses of the light hadrons ($Q \sim 1\text{GeV}$). This could be an indication that the confinement of quarks and gluons inside hadrons is actually a consequence of the growth of the coupling at low scale, which is a corollary of the decrease at high scales that leads to asymptotic freedom.

Thanks to the definition of Λ_{QCD}^2 , one can write:

$$\alpha_s(Q^2) = \frac{\alpha_s(\mu^2)}{1 + b_0\alpha_s(\mu^2) \left(\ln\left(\frac{Q^2}{\Lambda_{QCD}^2}\right) + \ln\left(\frac{\Lambda_{QCD}^2}{\mu^2}\right) \right)} = \quad (1.14)$$

$$= \frac{\alpha_s(\mu^2)}{1 + b_0\alpha_s(\mu^2)\ln\left(\frac{Q^2}{\Lambda_{QCD}^2}\right) + b_0\alpha_s(\mu^2)\ln\left(\frac{\Lambda_{QCD}^2}{\mu^2}\right)} \quad (1.15)$$

and, using condition (1.13), one gets:

$$\alpha_s(Q^2) = \frac{1}{b_0\ln\left(\frac{\Lambda_{QCD}^2}{\mu^2}\right)}. \quad (1.16)$$

1.2 QCD beyond leading order

In this section I will introduce the main properties of QCD beyond the leading order, from factorization (section 1.2.1) to DGLAP equation (section 1.2.2).

1.2.1 The factorization theorem in DIS

In the previous section the dynamics of coloured particles have been briefly described, but the particles we have to deal with in experiments, namely hadrons, are colour singlets. When the energy scale is large enough, it is possible to think of hadrons' interaction as the interaction between their constituents. Thanks to the running of the coupling constant, QCD enables one to calculate the *partonic* cross sections, through the perturbative Feynman diagram technique. Nevertheless, this is not enough to predict experimental observables. In fact, when we study processes involving hadrons, we need to combine the probability of the partons' transition from the initial state to the final one and the probability of finding partons in the hadrons, with momentum and quantum numbers adequate to originate the process we are studying. As already announced in the introduction, this goal can be reached through the *collinear factorization theorem* in equation (4). In this section I will obtain a proof of this classical result of QCD in the context of DIS.

The kinematical variables of DIS have been already defined in (2). Now I will calculate the cross section for such a process.

The DIS matrix element has the form:

$$i\mathcal{T} = (-ie)\bar{u}(k')\gamma^\mu u(k)\frac{i}{Q^2}(ie)\int d^4xe^{iq\cdot x}\langle X | J_\mu(x) | P \rangle, \quad (1.17)$$

where J_μ is the quark electromagnetic current and the hadronic matrix element is between the proton and some high-energy hadron state. The square amplitude, summed over all the possible final states and averaged over spins, is

$$\begin{aligned} |\mathcal{T}|^2 &= \frac{e^4}{Q^4}\frac{1}{4}\text{Tr}(k\gamma^\mu k'\gamma^\nu)\sum_X\int d^4xe^{iq\cdot x}\langle P | J_\mu(0) | X \rangle\langle X | J_\nu(x) | P \rangle = \\ &= \frac{e^4}{Q^4}L_{\mu\nu}\cdot W^{\mu\nu}, \end{aligned} \quad (1.18)$$

namely, it is the contraction between a leptonic tensor $L_{\mu\nu}$ and a hadronic tensor $W^{\mu\nu}$. The first has the familiar QED expression:

$$L^{\mu\nu} = 2(k^\mu k'^\nu + k^\nu k'^\mu - g^{\mu\nu}k\cdot k'); \quad (1.19)$$

the hadronic tensor, on the contrary, is unknown and parametrizes our ignorance of nucleon's structure. It is possible however to find a convenient expression for

$W^{\mu\nu}$, using the known features of field theory and electromagnetic interaction. Thus, imposing symmetry ($W^{\mu\nu} = W^{\nu\mu}$), parity invariance and Ward identities ($q_\mu W^{\mu\nu} = q_\nu W^{\mu\nu} = 0$), the hadronic tensor takes the form:

$$W^{\mu\nu} = \left(-g^{\mu\nu} + \frac{q^\mu q^\nu}{q^2}\right) F_1(x, Q^2) + \left(p^\mu - q^\mu \frac{p \cdot q}{q^2}\right) \left(p^\nu - q^\nu \frac{p \cdot q}{q^2}\right) \frac{F_2(x, Q^2)}{p \cdot q}, \quad (1.20)$$

where now our ignorance is summarized in the structure functions $F_1(x, Q^2)$ and $F_2(x, Q^2)$. Substituting equations (1.19) and (1.20) in the DIS square amplitude (1.18) and rewriting the usual Lorentz invariant phase space in terms of x and Q^2 , we obtain the DIS differential cross-section:

$$\frac{d\sigma}{dx dQ^2} = \frac{1}{2s^2} \frac{e^4}{x^2 Q^2} \left[F_1(x, Q^2) + F_2(x, Q^2) \frac{s}{Q^2} \left(x \frac{s}{Q^2} - 1 \right) \right]. \quad (1.21)$$

Now, let's focus on the hadronic tensor $W^{\mu\nu}$. The optical theorem allows us to express it in terms of the *forward Compton amplitude* of the proton:

$$W^{\mu\nu} = \mathbf{Im} \int d^4x e^{iq \cdot x} \langle P | T \{ J^\mu(0) J^\nu(x) \} | P \rangle. \quad (1.22)$$

In analogy with equation (1.20), we can write

$$T^{\mu\nu} = \int d^4x e^{iq \cdot x} \langle P | T \{ J^\mu(0) J^\nu(x) \} | P \rangle = (-g^{\mu\nu} + \dots) \tilde{F}_1 + (p^\mu p^\nu + \dots) \tilde{F}_2, \quad (1.23)$$

where

$$F_i(x, Q^2) = 2 \mathbf{Im} \tilde{F}_i(x, Q^2). \quad (1.24)$$

The T-ordered product can be expanded, using the Wilson expansion, because we are in the kinematical region of DIS (namely, $Q^2 \rightarrow \infty$ and $x \rightarrow 0$). In this way we can factorize the high-energy dependence in the coefficients of the expansion, which is organized according to the operator spin, namely the number of Lorentz indices, provided that each operator is symmetric and traceless:

$$T \{ J^\mu(0) J^\nu(x) \} = \sum_s C_{\mu_1 \dots \mu_{s-2}}^s(x) O_s^{\mu\nu\mu_1 \dots \mu_{s-2}}. \quad (1.25)$$

Provided that the operator O_s has mass dimension equal to $d_{\mathcal{O}}$, the coefficient functions C_s has the dimension $(mass)^{6-d_{\mathcal{O}}}$.

To get an expression of $T^{\mu\nu}$ from (1.25), we need to Fourier transform it. Then, extracting also the vectorial dependence from the coefficients C_s , we get:

$$T^{\mu\nu} = \langle P|T\{\mu(-q^2)J^\nu(q^2)\}|P\rangle = \sum_s \langle P|\mathcal{O}_s^{\mu\nu\mu_1\dots\mu_{s-2}}|P\rangle \frac{2q_{\mu_1}}{Q^2} \dots \frac{2q_{\mu_{s-2}}}{Q^2} C_s(Q^2) \quad (1.26)$$

where now the coefficients $C_s(Q^2)$ have dimension $(mass)^{-d_{\mathcal{O}}+s}$. To find a convenient expression for the matrix element of $\mathcal{O}_s^{\mu\nu\mu_1\dots\mu_{s-2}}$ we observe that for each Lorentz index of the operator, we will have a Lorentz index in the expectation value in the proton state. Since the q^μ dependence is only in the coefficients of the expansion, this Lorentz index must be carried by the proton momentum p^μ . The matrix element can thus be written as:

$$\langle P|\mathcal{O}_s^{\mu\nu\mu_1\dots\mu_s}|P\rangle = 2 A_s p^\mu p^\nu p^{\mu_1} \dots p^{\mu_{s-2}}, \quad (1.27)$$

where A_s are constants which carry non trivial informations about proton structure. Their dimension is $(mass)^{d_{\mathcal{O}}-s}$.

Substituting the latter matrix element in equation (1.26), we obtain

$$T^{\mu\nu} = \sum_s A_s c_s(Q^2) 4 p^\mu p^\nu \left(\frac{2p \cdot q}{Q^2}\right)^{s-2}, \quad (1.28)$$

where we have separated the kinematical and dynamical parts of the hadronic tensor ($C_s(Q^2)$) from the one depending on the proton structure (A_s).

The leading terms of expansions (1.28) can be found through dimensional analysis. The dimension of A_s is carried by the proton mass, while the dimension of C_s is carried by Q^2 . So, recalling that $x = \frac{Q^2}{2p \cdot q}$, the contribution of the operator \mathcal{O}_s in the proton state can be estimated as

$$\langle P|C_{\mu_1\dots\mu_s} \mathcal{O}_s^{\mu\nu\mu_1\dots\mu_{s-2}}|P\rangle \sim x^{-s+2} \left(\frac{m_p}{Q}\right)^{d_{\mathcal{O}}-s}. \quad (1.29)$$

Thus, the relative contribution of an operator is controlled by its *twist* ($t = d_{\mathcal{O}} - s$). As long as $Q^2 \gg m_p$, the lower twist operators ($t = 2$) dominate.

Now let us focus on \tilde{F}_2 in equation (1.23). From the previous calculations we can write:

$$\tilde{F}_2 = 2 \sum_s \left(\frac{2p \cdot q}{Q^2}\right)^{s-1} c_s(Q^2) A_s. \quad (1.30)$$

Equation (1.30) can be viewed as a Taylor series in $\omega = \frac{1}{x}$. In the leading twist approximation, Cauchy's theorem enables us to extract the product $A_s C_s$:

$$2C_s A_s = \int_{\Gamma} \frac{d\omega}{2\pi i} \tilde{F}_2(\omega) \omega^{-s}, \quad (1.31)$$

where the integration path Γ is a circle around the origin, small enough to avoid the physical singularities in $\omega > 1$ and $\omega < 1$. We can deform Γ to the path Γ' in Figure 1.4, which passes just above and just below the singularity cut. The integral (1.31), neglecting contributions from the large circle and changing variable from ω to x , becomes:

$$\begin{aligned} 2C_s A_s &= \int_0^1 \frac{dx}{2\pi i} x^{s-2} \left(\tilde{F}_2(x+i\epsilon) - \tilde{F}_2(x-i\epsilon) \right) = \\ &= \int_0^1 \frac{dx}{2\pi} x^{s-2} 2\mathbf{Im} \tilde{F}_2(x) = \int_0^1 \frac{dx}{2\pi} x^{s-1} \frac{F_2(x, Q^2)}{x}. \end{aligned} \quad (1.32)$$

In the last equality we used Schwartz reflection principle $\tilde{F}_2(z) = \tilde{F}_2^*(z^*)$. The

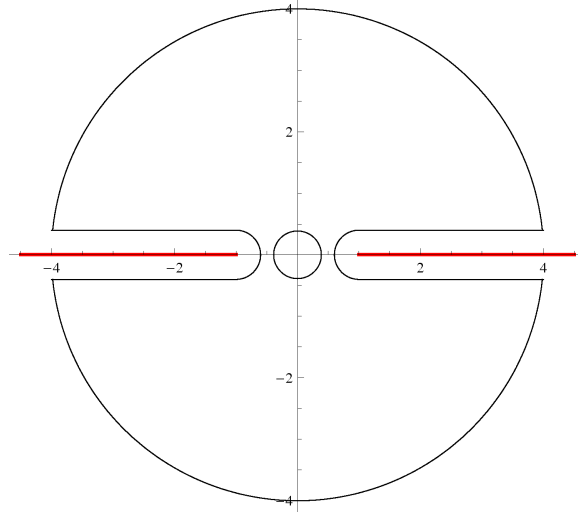


Figure 1.4: The integration contours Γ and Γ' in the ω complex plane. Both paths are oriented counterclockwise. Physical singularity cuts are marked in red.

result in equation (1.32) is called dispersion integral.

If we define the Mellin transform

$$\mathcal{M}[f(x)](N) = \int_0^1 dx x^{N-1} f(x) \quad (1.33)$$

and its inverse transform

$$f(x) = \int_C \frac{dN}{2\pi i} x^{-N} \mathcal{M}[f(x)](N), \quad (1.34)$$

equation (1.32) tells us that the s -th contribution to Wilson expansion is the Mellin moment of $\frac{F_2(x, Q^2)}{x}$, where $F_2(x, Q^2)$ is the physical structure function. Inverting (1.32) and substituting s by the usual Mellin moment variable N , we get:

$$F_2(x, Q^2) = x \int_C \frac{dN}{2\pi i} x^{-N} C_N(x, N) A_N. \quad (1.35)$$

Now we define also $C_N(Q^2)$ and A_N as Mellin transform as follows:

$$C_N(Q^2) = \int_0^1 C(x, Q^2) x^{N-1} dx \quad (1.36)$$

$$A_N = \int_0^1 q(x) x^{N-1}, \quad (1.37)$$

where $C(x, Q^2)$ is called *coefficient function* and $q(x)$ is the *parton distribution function* (PDF). The meaning of these two new quantities is clear from the way we obtained them: $q(x)$ encloses the information on proton structure and is process-independent; while $C(x, Q^2)$ is linked to the dynamic of parton and can be calculated through QCD.

Substituting equations (1.36) and (1.37) in (1.35), we obtain, via the properties of Mellin convolution, the *factorization theorem* for one active quark flavour:

$$F_2(x, Q^2) = x \int_x^1 \frac{dy}{y} C\left(\frac{x}{y}, Q^2\right) q(y) = C \otimes q. \quad (1.38)$$

The meaning of the result (1.38) is that we can actually calculate the physical observables through the convolution between coefficient functions and PDFs .

The story, though, hasn't still come to its end: if we actually want to predict physical observables using the *factorization theorem* equation (1.38), we run into some complications, related to the need to determine the still unconstrained Q^2 dependence of coefficient functions, as will become clear in the next section.

1.2.2 DGLAP equation

In order to get a deeper understanding of the result (1.38), it is useful to perform the explicit calculation of the coefficient functions (1.36) using QCD Feynman rules.

Let us consider the tree process in Figure 1.5 of a free quark interacting with a virtual photon. We parametrize the quark momentum p , distinguishing its lon-

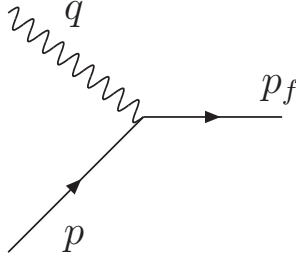


Figure 1.5: Interaction of a virtual photon with a quark

itudinal and transverse components, through the *Sudakov parametrization*:

$$p = x\rho + y\eta + \bar{p}_T \quad \text{where} \quad \begin{cases} \rho^2 = \eta^2 = 0 \\ 2\rho \cdot \eta = 1 \\ \bar{p}_T \cdot \rho = \bar{p}_T \cdot \eta = 0 \end{cases} . \quad (1.39)$$

x and y give the longitudinal motion of the quark, while \bar{p}_T gives the transverse motion. If the quark is on-shell we have:

$$p^2 = m_q^2 = -|\bar{p}_T|^2 + 2\rho \cdot \eta xy \Rightarrow y = \frac{m_q^2 + |\bar{p}_T|^2}{2\rho \cdot \eta x}. \quad (1.40)$$

We can assume $\bar{p}_T = 0$ and neglect m_q , then $y = 0$ and, from momentum conservation, $x = \frac{Q^2}{2p \cdot q} = 1$.

Performing the QED calculation of the square amplitude, we get the quark structure function at first order:

$$F_2^q(x, Q^2) = e_i^2 \delta(x - 1), \quad (1.41)$$

where e_i is the quark charge. We are dealing with a free quark, then, recalling equation (1.35), we can say that $A_N = 1$ and identify C_N with the Mellin transform of F_2^q .

Now let us go on to the first order in α_s and consider the diagram in Figure 1.6, where the quark emits a gluon, before interacting with the photon. In this case we can not assume that $\bar{p}'_T = 0$, because of the gluon emission. Let us write the gluon momentum k and the momentum flowing in the quark propagator p' , using the parametrization (1.39):

$$k = (1 - z)p + \bar{k}_T + y\eta \quad (1.42)$$

$$p' = (p - k) = zp - \bar{k}_T - y\eta \quad (1.43)$$

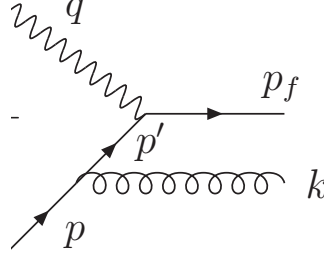


Figure 1.6: Real gluon emission diagram in DIS

As the gluon is real, we have $k^2 = 0$ and so $y = \frac{|\bar{k}_T|^2}{2\rho\eta(1-z)}$. Thus:

$$p'^2 = -|\bar{k}_T|^2 - 2\rho\eta y z = -|\bar{k}_T|^2 - \frac{|\bar{k}_T|^2 z}{1-z} = -\frac{|\bar{k}_T|^2}{1-z}. \quad (1.44)$$

As \bar{k}_T goes to zero, p'^2 goes on shell, giving rise to a collinear divergence in the fermion propagator and thus in the quark structure function. Regulating the collinear divergence with a (factorization) scale μ^2 , the final result of the calculation is

$$F_2^q = e_q^2 x \left[\delta(1-x) + \frac{\alpha_s}{2\pi} \left(P(x) \ln \frac{Q^2}{\mu^2} \right) \right], \quad (1.45)$$

where we have introduced the *splitting function* $P(x)$, that can be seen as the probability that a quark, having radiated a gluon, is left with the fraction x of its original momentum. More details on splitting function and factorization scale will be given below.

If one removes the scale, by leading $\mu^2 \rightarrow 0$ a collinear singularity appears. The presence of such singularities spoil the result of the previous section, because they lead to predict for physical observables infinite values.

We can understand the meaning of such divergences, recalling that in QCD the perturbative approach is consistent only if $\alpha_s(Q^2) \ll 1$; what we have been saying so far is that the quark is free, but actually this situation never happens, due to confinement. So we need to define a reference scale μ^2 , at which a quark is a bare fermion, namely where the coefficients $A_N(\mu^2) = 1$. From this observation we can derive the scaling violation (Q^2 dependence) of the quark structure function (1.41): $C(x, Q^2)$ can depend on Q^2 only through a factorization scale μ^2 , that is $C(x, \frac{Q^2}{\mu^2})$.

At the factorization scale, the result (1.38) can be written in Mellin space as:

$$\int dx x^{N-1} \frac{F_2(x, Q^2)}{x} = C_N \left(\frac{Q^2}{\mu^2} \right) A_N(\mu^2). \quad (1.46)$$

Now, the physical observables must not depend on the factorization scale, thus we have to impose:

$$\mu^2 \frac{d}{d\mu^2} C_N \left(\frac{Q^2}{\mu^2} \right) A_N(\mu^2) = 0. \quad (1.47)$$

As is clear from (1.47), also A_N , thus PDFs, must depend on the factorization scale. Moreover the two dependences on μ^2 of C_N and A_N must balance, that is:

$$-\frac{1}{C_N} \mu^2 \frac{d}{d\mu^2} C_N \left(\frac{Q^2}{\mu^2} \right) = \frac{1}{A_N} \mu^2 \frac{d}{d\mu^2} A_N(\mu^2) \equiv \gamma_N(\alpha_s(\mu^2)), \quad (1.48)$$

where $\gamma_N(\alpha_s(\mu^2))$ is the *anomalous dimension* of the operator \mathcal{O}_N of Wilson expansion (1.25).

The $\gamma_N(\alpha_s(\mu^2))$'s can depend on the scale only through $\alpha_s(\mu^2)$ because they must be dimensionless. This fact allows the logarithmic derivative of C_N and A_N to be computed perturbatively.

The expression (1.48) contains the evolution equations for A_N and C_N , with the scale μ^2 :

$$\frac{1}{A_N} \mu^2 \frac{d}{d\mu^2} A_N(\mu^2) = \gamma_N(\alpha_s(\mu^2)) \quad (1.49)$$

$$\frac{1}{C_N} \mu^2 \frac{d}{d\mu^2} C_N \left(\frac{Q^2}{\mu^2} \right) = -\gamma_N(\alpha_s(\mu^2)). \quad (1.50)$$

Their general solutions are respectively:

$$A_N(Q^2) = A_N(\mu^2) \exp \left(\int_{\alpha_s(\mu^2)}^{\alpha_s(Q^2)} d\alpha \frac{\gamma_N(\alpha)}{\beta(\alpha)} \right) = A_N(\mu^2) \Gamma(Q^2, \mu^2) \quad (1.51)$$

$$C_N \left(\frac{Q^2}{\mu^2}, \alpha_s(\mu^2) \right) = C_N(1, \alpha_s(Q^2)) \Gamma(Q^2, \mu^2),$$

where $\Gamma(Q^2, \mu^2)$ is called *evolution kernel*.

With many active flavour, equation (1.49) becomes the DGLAP equation in Mellin space:

$$\mu^2 \frac{d}{d\mu^2} \begin{pmatrix} A_N^i(\mu^2) \\ A_N^g(\mu^2) \end{pmatrix} = \begin{pmatrix} \gamma_{q_i q_j}(N, \alpha_s(\mu^2)) & \gamma_{q_i g}(N, \alpha_s(\mu^2)) \\ \gamma_{g q_j}(N, \alpha_s(\mu^2)) & \gamma_{g g}(N, \alpha_s(\mu^2)) \end{pmatrix} \begin{pmatrix} A_N^j(\mu^2) \\ A_N^g(\mu^2) \end{pmatrix} \quad (1.52)$$

If we introduce the *splitting function* as the inverse Mellin transform (1.34) of the anomalous dimension

$$P(x, \alpha_s) = \frac{1}{2\pi i} \int_{c-i\infty}^{c+i\infty} dN n^{-N} \gamma(N, \alpha_s(\mu^2)), \quad (1.53)$$

we can write DGLAP equation in ordinary space as follows

$$\mu^2 \frac{d}{d\mu^2} \begin{pmatrix} q^i(x, \mu^2) \\ g(x, \mu^2) \end{pmatrix} = \frac{\alpha_s}{2\pi} \begin{pmatrix} P_{q_i q_j}(x, \alpha_s(\mu^2)) & P_{q_i g}(x, \alpha_s(\mu^2)) \\ P_{g q_j}(x, \alpha_s(\mu^2)) & P_{g g}(x, \alpha_s(\mu^2)) \end{pmatrix} \otimes \begin{pmatrix} q^j(x, \mu^2) \\ g(x, \mu^2) \end{pmatrix}. \quad (1.54)$$

Leading Order solution to DGLAP equation

The solution of DGLAP equation can be computed at different order in perturbation theory. In this section I will compute the evolution kernels of equation (1.51), at the Leading Order (LO), with one active flavour.

The expression for $\Gamma_N(Q^2, \mu^2)$ is:

$$\Gamma_N(Q^2, \mu^2) = \exp \left(\int_{\alpha_s(\mu^2)}^{\alpha_s(Q^2)} d\alpha \frac{\gamma_N(\alpha)}{\beta(\alpha)} \right) \quad (1.55)$$

Expanding perturbatively γ_N and β as:

$$\gamma_N(\alpha_s) = \alpha_s \gamma_0(N) + O(\alpha_s^2), \quad \beta(\alpha_s) = -b\alpha_s^2 + O(\alpha_s^3) \quad (1.56)$$

we get:

$$\begin{aligned} \Gamma_N(Q^2, \mu^2) &= \exp \left(-\frac{\gamma_0(N)}{b} \int_{\alpha_s(\mu^2)}^{\alpha_s(Q^2)} \frac{d\alpha}{\alpha} \right) \\ &= \left(\frac{\alpha_s(Q^2)}{\alpha_s(\mu^2)} \right)^{-\frac{\gamma_0(N)}{b}} = \left(1 + b\alpha_s(Q^2) \ln \left(\frac{Q^2}{\mu^2} \right) \right)^{\frac{\gamma_0(N)}{b}}. \end{aligned} \quad (1.57)$$

It is clear from (1.57) that LO DGLAP equation resums all the leading logarithms (LL), i.e. all the terms of the form $\left(\alpha_s(Q^2) \ln \left(\frac{Q^2}{\mu^2} \right) \right)^k$. In effect these terms must be included as they are of order one, because $\alpha_s \sim \frac{1}{\ln \left(\frac{Q^2}{\mu^2} \right)}$. It is easy to see that NLO DGLAP equation resums the NLL, i.e. all the terms of the form $\alpha_s \left(\alpha_s(Q^2) \ln \left(\frac{Q^2}{\mu^2} \right) \right)^k$, and so on.

Now let us find the LO expression for $C_N\left(\frac{Q^2}{\mu^2}, \alpha_s(\mu^2)\right)$. We need to write the evolution kernel at LO:

$$\Gamma_N(Q^2, \mu^2) = 1 + \gamma_0(N)\alpha_s(Q^2)\ln\left(\frac{Q^2}{\mu^2}\right) + O(\alpha_s^2). \quad (1.58)$$

Substituting (1.58) into (1.51), we have:

$$\begin{aligned} C_N\left(\frac{Q^2}{\mu^2}, \alpha_s(\mu^2)\right) &= (C_0(N) + \alpha_s(Q^2)C_1(N))\left(1 + \gamma_0(N)\alpha_s(Q^2)\ln\left(\frac{Q^2}{\mu^2}\right)\right) \\ &= C_0 + C_0\alpha_s\gamma_0\ln\left(\frac{Q^2}{\mu^2}\right) + O\left(\alpha_s^2, \alpha_s\ln^0\left(\frac{Q^2}{\mu^2}\right)\right) \end{aligned} \quad (1.59)$$

Taking the Mellin transform of the last equation we have

$$C\left(x, \frac{Q^2}{\mu^2}, \alpha_s(\mu^2)\right) = C_0(x) + \alpha_s[P_0 \otimes C_0](x)\ln\left(\frac{Q^2}{\mu^2}\right) + O\left(\alpha_s^2, \alpha_s\ln^0\left(\frac{Q^2}{\mu^2}\right)\right). \quad (1.60)$$

Recalling that $C_0(x) = e_q^2\delta(1-x)$, we finally obtain:

$$C\left(x, \frac{Q^2}{\mu^2}, \alpha_s(\mu^2)\right) = e_q^2\left(\delta(1-x) + \alpha_s P_0(x)\ln\left(\frac{Q^2}{\mu^2}\right)\right). \quad (1.61)$$

Thus, the LO coefficient function coincides with the quark structure function of equation (1.45) and the LO splitting function is the coefficient of the logarithmic term $\ln\left(\frac{Q^2}{\mu^2}\right)$. $P_0(x)$ is the $P(x)$ of equation (1.45) and can be computed from the explicit calculation of the real gluon emission diagram in Figure 1.6.

The previous considerations can be generalized to all possible emissions $i \rightarrow j$ (with $i, j = q, g$) and we can then obtain a complete set of splitting functions.

In this chapter we studied the PDFs' dependence on the ratio $\frac{Q^2}{\mu^2}$; in the next chapter we will study in greater detail the dependence of PDFs on x and study, with particular attention to the small x region.

Chapter 2

Small x Resummation

The small x regime of QCD is the kinematic region in which hard process happens at a center-of-mass energy much larger than the hard scale of the process. As the energy available at hadron colliders, such as the LHC, increases, small x QCD becomes more and more relevant. The x parameter measures the ratio between the two large scales involved and its definition depends on the process we are studying. In this work I focus on DIS and then the hard scale is set by the virtuality of the photon Q^2 and, provided that p is the momentum of the hadron and q that of the virtual photon,

$$x = \frac{Q^2}{2p \cdot q} = \frac{Q^2}{s}(1 + O(x)). \quad (2.1)$$

In the previous chapter we saw that the relevance of DGLAP equation is related to the fact that, through it, we can perform the resummation to all orders of the large logarithm of the ratio between the hard scale of the process and factorization scale, $\frac{Q^2}{\mu^2}$. Now, we turn to high energy region, namely $s \gg Q^2$ and $x \rightarrow 0$, where terms of the form $\alpha_s \ln\left(\frac{1}{x}\right)$, present to all orders in perturbation theory, become of order 1 and have to be resummed.

In the present chapter I will present some general results on the small x behavior of PDFs' evolution equations and show some theoretical features of BFKL equation (section 2.1); then I will present the approach to small x resummation of the ABF group (section 2.2).

2.1 Small x evolution equations

In the previous chapter we obtained DGLAP equation and see that, when the number of active flavours is greater than one, the evolution of PDFs mixes quarks and gluons.

It is, then, convenient to rearrange the PDFs $q_i(x)$, $\bar{q}_i(x)$ and $g(x)$, defining *singlet* and *non singlet* quark distributions, as follows:

$$q_{NS} = q_i - q_j, \quad \{i, j\} = 1, \dots, n_f \quad (2.2)$$

$$q_S = \Sigma = \sum_i^{n_f} [q_i + \bar{q}_i]. \quad (2.3)$$

The evolution of q_{NS} , in fact, decouples and obey to the differential equation:

$$\mu^2 \frac{d}{d\mu^2} q_{NS}(x, \mu^2) = \frac{\alpha_s(\mu^2)}{2\pi} P(x, \alpha_s(\mu^2)) \otimes q_{NS}(x, \mu^2). \quad (2.4)$$

The evolution of the singlet distribution $\Sigma(x, \mu^2)$ is coupled to that of the gluon and obey to equation (1.54), which now takes the form:

$$\mu^2 \frac{d}{d\mu^2} \begin{pmatrix} \Sigma(x, \mu^2) \\ g(x, \mu^2) \end{pmatrix} = \frac{\alpha_s(\mu^2)}{2\pi} \begin{pmatrix} P_{qq}(x, \alpha_s(\mu^2)) & 2n_f P_{qg}(x, \alpha_s(\mu^2)) \\ P_{gq}(x, \alpha_s(\mu^2)) & P_{gg}(x, \alpha_s(\mu^2)) \end{pmatrix} \otimes \begin{pmatrix} \Sigma(x, \mu^2) \\ g(x, \mu^2) \end{pmatrix}. \quad (2.5)$$

In this section we will outline the crucial properties of the latter equation in the small x regime, beginning with some considerations on splitting functions and anomalous dimensions (section 2.1.1) and ending with the method thorough which one can actually get the solution of equation (2.5) at LL x accuracy (section 2.1.2).

2.1.1 Small x anomalous dimensions

In equations (2.6), (2.7), (2.8) and (2.9) the LO expressions of splitting functions are shown; while in equations (2.10), (2.11), (2.12) and (2.13) we give the LO expression of anomalous dimensions, for future applications.

$$P_{qq}^0(x) = C_F \left[\frac{1+x^2}{(1-x)_+} + \frac{3}{2} \delta(1-x) \right], \quad (2.6)$$

$$P_{qg}^0(x) = T_R [x^2 + (1-x)^2], \quad (2.7)$$

$$P_{gq}^0(x) = C_F \left[\frac{1+(1-x)^2}{x} \right], \quad (2.8)$$

$$P_{gg}^0(x) = 2C_A \left[\frac{1}{(1-x)_+} + \frac{1-x}{x} + x(1-x) \right] + \delta(1-x) \frac{11C_A - 4n_f T_R}{6} \quad (2.9)$$

$$\gamma_{qq}^0(N) = C_F \left[-\frac{1}{2} + \frac{1}{N(N+1)} - 2 \sum_{k=2}^N \frac{1}{k} \right], \quad (2.10)$$

$$\gamma_{gg}^0(N) = T_R \left[\frac{2 + N + N^2}{N(N+1)(N+2)} \right], \quad (2.11)$$

$$\gamma_{gq}^0(N) = C_F \left[\frac{2 + N + N^2}{N(N^2 - 1)} \right], \quad (2.12)$$

$$\gamma_{gg}^0(N) = 2C_A \left[-\frac{1}{12} + \frac{1}{N(N-1)} + \frac{1}{(N+1)(N+2)} - \sum_{k=2}^N \frac{1}{k} \right] + \frac{2}{3} n_f T_R. \quad (2.13)$$

At LO, then, P_{gg} and P_{gq} show a singular behavior at small x . From this fact it appears that the fixed order perturbation theory breaks down at small x , as the splitting functions are divergent. Before dealing with this question, let us study the behavior of the evolution equations in the small x region.

We will work in Mellin space, thus it is important to observe that the singularities that arise in the splitting functions when $x \rightarrow 0$, in the anomalous dimensions happen when $N \rightarrow 1$. To simplify the notation, we define the new distribution G and Q , as:

$$G = xg, \quad Q = xq. \quad (2.14)$$

The x factor, thanks to the properties of Mellin transform (1.33), turns into a shift in the argument of the new anomalous dimensions with respect to the old one:

$$\gamma_{AB}(N) = \gamma_{ab}(N+1). \quad (2.15)$$

It is possible to prove that small x DGLAP equation is dominated by the rightmost singularity of the anomalous dimension.

Therefore let us expand the LO anomalous dimensions around their leading singularity:

$$\gamma_{singlet} = \frac{1}{N} \begin{pmatrix} 0 & 0 \\ 2C_A & 2C_F \end{pmatrix} + \begin{pmatrix} 0 & \frac{4}{3}n_f T_R \\ -\frac{3}{2}C_F & \frac{11}{6}C_A - \frac{2}{3}n_f T_R \end{pmatrix} + O(N) \quad (2.16)$$

$$\gamma_{non-singlet} = \frac{C_F}{N+1} - \frac{C_F}{2} + O(N+1) \quad (2.17)$$

From the above relation it is evident that the singlet channel has the singularity shifted of one unit to the right with respect to the non-singlet one, which, then, has an extra power of x :

$$q_{NS} \sim xq_S \sim xg, \quad (2.18)$$

namely the LO non-singlet distribution at small x is subleading with respect to the singlet one. For this reason in the next we will focus most on the singlet distribution.

Now, let us diagonalize the matrix of anomalous dimensions in the singlet evolution equation (2.5). The eigenvalues are:

$$\gamma_{\pm} = \frac{1}{2} \left[\gamma_{gg} + \gamma_{qq} \pm \sqrt{(\gamma_{gg} - \gamma_{qq})^2 + 8n_f \gamma_{gq} \gamma_{qg}} \right] \quad (2.19)$$

and, at LO up to $O(N)$, they take the values:

$$\gamma_+ = 2C_A \frac{1}{N} + \left(\frac{11}{6} C_A - \frac{2}{3} n_f T_R + \frac{4}{3} \frac{C_F}{C_A n_f T_R} \right) \quad (2.20)$$

$$\gamma_- = -\frac{4}{3} \frac{C_F}{C_A} n_f T_R \quad (2.21)$$

Hence, LO γ_+ has a pole when $N \rightarrow 0$, while LO γ_- is regular.

From all these considerations, it is clear that, if we want to determine the correct behavior of the parton distributions at small x , we need to find the way to resum the large x logarithms.

In the asymptotic limit where $x \rightarrow 0$ and $Q^2 \rightarrow \infty$, LO DGLAP equation is sufficient, because it also resums all terms of the form $\alpha_s \ln\left(\frac{Q^2}{\mu^2}\right) \ln\left(\frac{1}{x}\right)$, namely the double leading-logarithms (DLL) series. When Q^2 is not so large, though, we need to consider also all the terms $\alpha_s \ln\left(\frac{1}{x}\right)$, not accompanied by a large $\ln\left(\frac{Q^2}{\mu^2}\right)$.

The resummation of these terms to all orders, retaining the full Q^2 dependence (and not only the leading $\ln(Q^2)$ terms), is accomplished by the Balitsky-Fadin-Kuraev-Lipatov (BFKL) equation. This result is obtained through high-energy factorization [4] and can be written in a form similar to the Mellin transform of DGLAP equation:

$$\frac{d}{d\xi} f(\xi, M) = \chi(M, \alpha_s) f(\xi, M), \quad (2.22)$$

where $\xi = \ln\left(\frac{1}{x}\right)$ and $f(\xi, M) = \int_{-\infty}^{+\infty} dt e^{-iMt} f(\xi, t)$, with $t = \ln\left(\frac{Q^2}{\mu^2}\right)$. It can be shown that the kernel $\chi(M, \alpha_s)$ is the inverse function of the DGLAP anomalous dimension $\gamma(N, \alpha_s)$.

To understand the physical difference between DGLAP and BFKL equation, we have to consider a Feynman diagram approach. The DGLAP evolution can be seen as a series that resums all the gluons emitted from a single quark (Figure 2.1). We saw, in the previous chapter, that one emission produces, in the collinear region, one power $\alpha_s \ln\left(\frac{Q^2}{\mu^2}\right)$; for multiple ladder emission we can produce all the terms of the series. The phase space integration of such diagrams is:

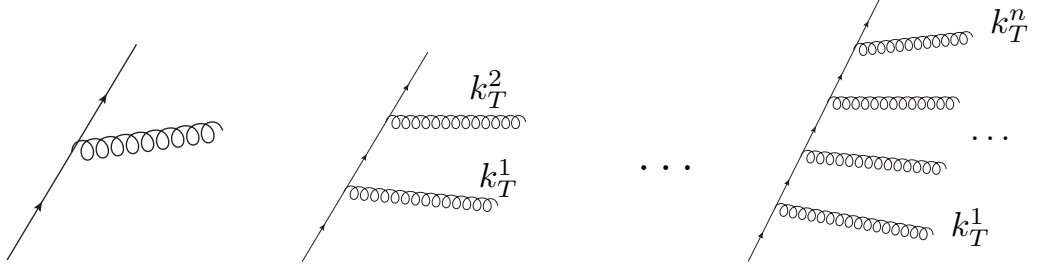


Figure 2.1: Gluon ladder emissions

$$\int_{\mu^2}^{Q^2} \frac{dk_{T_n}^2}{k_{T_n}^2} \int_{\mu^2}^{k_{T_n}^2} \frac{dk_{T_{n-1}}^2}{k_{T_{n-1}}^2} \cdots \int_{\mu^2}^{k_{T_3}^2} \frac{dk_{T_2}^2}{k_{T_2}^2} \int_{\mu^2}^{k_{T_2}^2} \frac{dk_{T_1}^2}{k_{T_1}^2} \sim \frac{[\ln(Q^2)]^n}{n!} \quad (2.23)$$

and the logarithms come from the strongly-ordered transverse momenta:

$$Q^2 \gg k_{T_n}^2 \gg \cdots \gg k_{T_1}^2. \quad (2.24)$$

In the BFKL case, instead, the relation (2.24) between transverse momenta isn't valid anymore, and the integration is taken over the full k_T phase space of the gluons.

2.1.2 The path-integral method to solve DGLAP equation

In section 1.2.2 we explained the method to find the solution to DGLAP equation at fixed order in perturbation theory (truncated solution). When we compute the splitting functions at a small x resummed level, we are including all the orders in α_s and thus a fixed order approach to the solution of DGLAP equation is not adequate anymore.

In this section I will outline the path-integral method, which allows us to compute the solution to DGLAP equation accounting for the α_s dependence to all orders.

The anomalous dimension matrix can be written as:

$$\gamma = \mathcal{M}_+ \gamma^+ + \mathcal{M}_- \gamma^-, \quad (2.25)$$

using the projectors (2.26) and (2.27) which have the form:

$$\mathcal{M}_+ = \frac{1}{\gamma^+ - \gamma^-} \begin{pmatrix} \gamma_{qq} - \gamma^- & \gamma_{qg} \\ X & \gamma^+ - \gamma_{qq} \end{pmatrix}, \quad (2.26)$$

$$\mathcal{M}_- = \frac{1}{\gamma^+ - \gamma^-} \begin{pmatrix} \gamma^+ - \gamma_{qq} & -\gamma_{qg} \\ -X & \gamma_{qq} - \gamma^- \end{pmatrix}, \quad (2.27)$$

where $X = (\gamma^+ - \gamma_{qq})(\gamma_{qq} - \gamma^-)/\gamma_{qg}$. With this formalism we get for the evolution kernels the following expression:

$$\Gamma(N, t_0, t) = \mathcal{P} \exp \left[\int_{t_0}^t dt' (\mathcal{M}_+(t')\gamma^+ + \mathcal{M}_-(t')\gamma^-) \right], \quad (2.28)$$

where the symbol \mathcal{P} stands for *path-integral*, namely we need to perform the integration maintaining the order of $\mathcal{M}_+(t)$ and $\mathcal{M}_-(t)$ because they do not commute for $t_1 \neq t_2$. Now let us find a more convenient form for (2.28):

$$\begin{aligned} \Gamma(N, t_0, t) &= \mathcal{P} \exp \left[\int_{t_0}^t dt' (\mathcal{M}_+(t')\gamma^+ + \mathcal{M}_-(t')\gamma^-) \right] = \\ &= \mathcal{P} \exp \left[\sum_{M=1}^N \int_{t_{M-1}}^{t_M} dt' (\mathcal{M}_+(t')\gamma^+ + \mathcal{M}_-(t')\gamma^-) \right] \end{aligned} \quad (2.29)$$

Now, if the number of intervals N is large enough, $\Delta t = \frac{t-t_0}{N}$ is small and thus, provided that $t_M = \frac{t_{M+1}-t_M}{2}$ we can write:

$$\begin{aligned} \Gamma(N, t_0, t) &= \mathcal{P} \exp \left[\sum_{M=1}^N \int_{t_{M-1}}^{t_M} dt' (\mathcal{M}_+(t')\gamma^+ + \mathcal{M}_-(t')\gamma^-) \right] \sim \\ &\sim \mathcal{P} \exp \left[\sum_{M=1}^N \Delta t (\mathcal{M}_+(t_M)\gamma^+ + \mathcal{M}_-(t_M)\gamma^-) \right] = \\ &= \prod_{M=1}^N \exp [\Delta t (\mathcal{M}_+(t_M)\gamma^+ + \mathcal{M}_-(t_M)\gamma^-)]. \end{aligned} \quad (2.30)$$

Now, thanks to the projectors' properties of \mathcal{M}_\pm , we have:

$$\begin{aligned} e^{\mathcal{M}_+\gamma^+\Delta t} &= \mathbb{1} + \mathcal{M}_+\gamma^+\Delta t + \frac{\mathcal{M}_+\mathcal{M}_+\gamma^+\gamma^+(\Delta t)^2}{2} + \dots = \\ &= \mathbb{1} + \mathcal{M}_+ \left(\gamma^+\Delta t + \frac{(\gamma^+\Delta t)^2}{2} + \frac{(\gamma^+\Delta t)^3}{3} + \dots \right) = \\ &= \mathbb{1} + \mathcal{M}_+(e^{\gamma^+\Delta t} - 1). \end{aligned} \quad (2.31)$$

Using the previous result, we can write (2.28) in the following way:

$$\begin{aligned}\Gamma(N, t_0, t) &= \prod_{M=1}^N [\mathbb{1} + \mathcal{M}_+(t_M)(e^{\gamma+\Delta t} - 1)] [\mathbb{1} + \mathcal{M}_-(t_M)(e^{\gamma-\Delta t} - 1)] = \quad (2.32) \\ &= \prod_{M=1}^N (\mathcal{M}_+(t_M)e^{\gamma+\Delta t} + \mathcal{M}_-(t_M)e^{\gamma-\Delta t}).\end{aligned}$$

2.2 ABF approach to small x resummation

In order to fix the small x instability of the evolution equations, we need to find a reasonable manner to compute the evolution kernels, taking into account the large logarithm of x .

In this section we will follow the approach of Altarelli, Ball and Forte (ABF) [1], showing first (section 2.2.1) the main ingredients for a stable small x resummation and then (section 2.2.2) some phenomenological results of this approach, which have been confirmed by other groups.

2.2.1 The three ingredients for stable small x resummation

We will consider the case of $n_f = 0$, in which there is a single parton distribution, the gluon distribution $G(\xi, t)$, with $\xi = \ln\left(\frac{1}{x}\right)$ and $t = \ln\left(\frac{Q^2}{\mu^2}\right)$. Defining the Mellin transforms:

$$G(N, t) = \int_0^\infty d\xi e^{-N\xi} G(\xi, t) \quad (2.33)$$

$$G(\xi, M) = \int_{-\infty}^\infty dt e^{-Mt} G(\xi, t) \quad (2.34)$$

we can rewrite both the DGLAP and BFKL equations in the following form:

$$\frac{d}{dt} G(N, t) = \gamma(N, \alpha_s) G(N, t) \quad (2.35)$$

$$\frac{d}{d\xi} G(\xi, M) = \chi(M, \alpha_s) G(\xi, M) \quad (2.36)$$

where γ and χ are related by the duality equations:

$$\begin{aligned}\chi(\gamma(N, \alpha_s), \alpha_s) &= N \\ \gamma(\chi(M, \alpha_s), \alpha_s) &= M\end{aligned} \quad (2.37)$$

which map the perturbative expansion of γ in powers of α_s at fixed N in the expansion of χ in powers of α_s at fixed M and conversely.

From equation (2.37) we obtain the first ingredient for a stable small x resummation: the *double leading expansion*, shown in Figure 2.2. As known, the anomalous

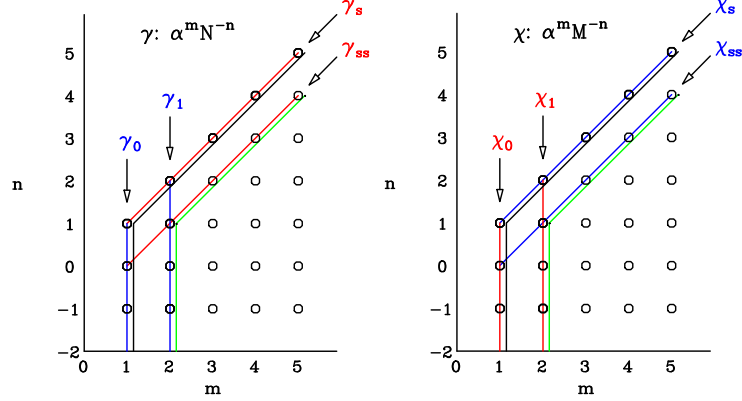


Figure 2.2: Double leading expansion of the GLAP anomalous dimension γ (left) and the BFKL kernel χ (right)

dimension can be seen as a series in α_s (DGLAP expansion):

$$\gamma(N, \alpha_s) = \alpha_s \gamma_0 + \alpha_s^2 \gamma_1 + \dots \quad (2.38)$$

Each coefficient γ_i in turn is a function of N , which contains the singularities we want to account for:

$$\gamma_i(N) = \frac{c_{-i}}{N^i} + \frac{c_{-i+1}}{N^{i-1}} + \dots + \frac{c_{-1}}{N} + c_i + c_1 N + \dots \quad (2.39)$$

The double leading expansion lies in a rearrangement of the terms of expansions (2.38) and (2.39), such that, for example at the leading order, the leading singularities of all γ_i are included in a new coefficient called γ_s . Using either the double-leading χ or the double-leading γ in the BFKL or DGLAP equation respectively leads, to the inclusion of all the terms which are logarithmically enhanced either in $\frac{1}{x}$ or in Q^2 to the given order. The result is shown in Figure (2.3): when $M \rightarrow 0$ it is near to the DGLAP one, while, when $N \rightarrow 0$, it is close to the BFKL one. Note the instability of the result when $N \rightarrow 0$, due to the instability of the BFKL kernel. To treat this poor behavior when $N \rightarrow 0$, we introduce the second ingredient.

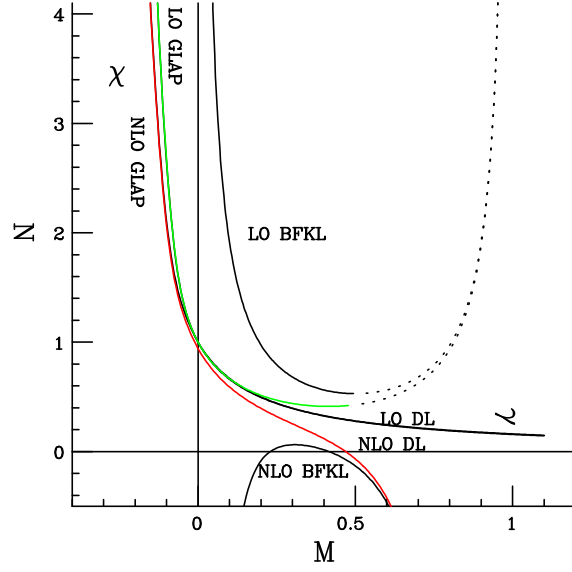


Figure 2.3: The BFKL kernel and its dual DGLAP anomalous dimension computed at LO and NLO in the BFKL expansion, the DGLAP expansion and the double-leading expansion

The BFKL kernel must be symmetric upon the interchange $M \rightarrow M - 1$, due to the symmetry of the three-gluon vertex upon the interchange of the radiated and radiating gluon. From Figure 2.3 is clear that this symmetry is manifest at LO level, while is broken at NLO level by terms that can be computed exactly, which come from running coupling effects and choice of DIS kinematic [1]. Hence, we can symmetrize the double-leading expansion by undoing the symmetry breaking terms, symmetrize the result and then restore the symmetry breaking kinematics and choose the argument of α_s . Following this way we get a very stable result, shown in Figure 2.4. The stability is related to the fact that χ must have a minimum at all orders, due to some important constraints on anomalous dimension:

- From momentum conservation, it follows that $\gamma(1, \alpha_s) = 0$ and, by duality, $\chi(0, \alpha_s) = 1$;
- As a consequence of the fact that the gluon loses momentum radiating, $\gamma(N, \alpha_s)$ decreases monotonically when N increases.

From Figure 2.4, we can define, for future application, the intercept of χ , as the point at which χ crosses $M = 0$.

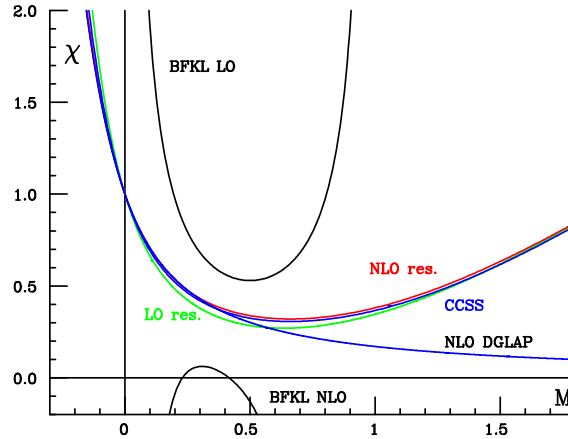


Figure 2.4: The LO and NLO resummed symmetrized double-leading kernels compared with LO and NLO BFKL kernels and NLO DGLAP kernels. CCSS denotes the result of an other approach to resummation [5]

The third ingredient for a stable small x resummation is the inclusion of the running coupling. In fact, it can be shown that the asymptotic behavior of the anomalous dimension when $x \rightarrow 0$ is determined by the position of the intercept of χ , which changes order by order. Hence, the correction to the position of the minimum of χ are asymptotically large when $\xi \rightarrow \infty$. Thanks to the presence of the kernel's minimum to all orders, the BFKL equation can be solved at running coupling level. This fact is crucial, because it corrects the duality equation with a finite numbers of terms which diverge as $\xi \rightarrow \infty$. The resummation of such terms can be performed exactly for the series of terms which grow fastest as $\xi \rightarrow \infty$ and the result can be expressed in terms of Bateman functions for a kernel with a generic dependence on α_s . The inclusion of Bateman anomalous dimension, i.e. the divergent terms related to running coupling, changes the leading singularity from a square root branch cut to a simple pole. Hence now the singularity is given by the pole of Bateman anomalous dimension; the position and the residue of Bateman pole are fully determined by the intercept and the curvature of the minimum of the original kernel, and their dependence on α_s . From Figure 2.5 we can see that, while in the NLO BFKL kernel the position of singularity grows linearly with α_s , in the resummed case the behavior of the position of the singularity is no longer linear and the slope is smaller.

Finally, to find the resummed anomalous dimension, we need to sum the Bateman contributions and subtract the double-counting terms. Then, via Mellin in-

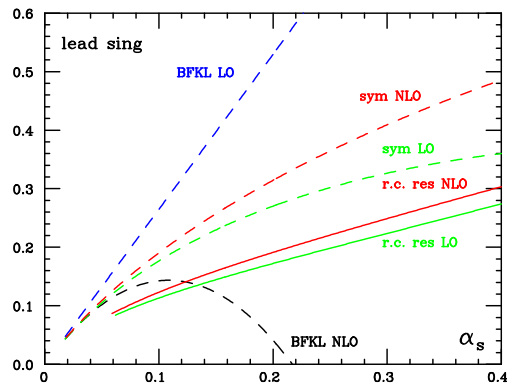


Figure 2.5: Leading small x singularity versus α_s

version, we obtain the resummed splitting function, shown in Figure 2.6. The resummed expansion is seen to be stable (the LO and NLO results are close) and matches the GLAP in the large $x > 0.1$ region, but at small x is free of the instability which the GLAP expansion shows already at NNLO. In Figure 2.7 the

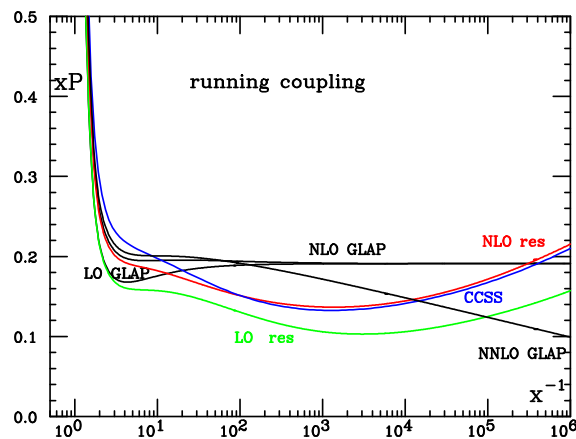


Figure 2.6: Resummed splitting function with running coupling

relative importance of various contribution is shown, by comparing the slope of resummed running-coupling splitting function with respect to ξ , to that of NLO GLAP result and that of the splitting function obtained by inverse Mellin transform of Bateman anomalous dimension. We can see that the behavior at small x is determined by the Bateman splitting function, while at large x the NLO DGLAP expansion dominates.

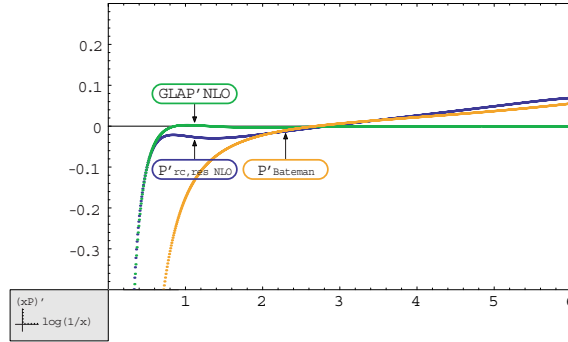


Figure 2.7: The slope of the splitting function with respect to ξ

2.2.2 Phenomenological results

To get the resummed physical observables, as stressed in Chapter 1, we need both PDFs at the scale Q^2 and coefficients functions. Hence, going from the resummation of evolutions equation to the resummation of physical observables, first we need to include the quark sector, extending the resummation to the case where $n_f \neq 0$, and then we need to resum also the coefficients functions.

As already said, the non singlet distribution is subleading compared to the singlet one (see equation (2.18)) and the splitting function matrix has only one singular eigenvalue at small x (see equation (2.20)). Hence, we can choose a factorization scheme in which only the singular terms as $N \rightarrow 0$ are included in the anomalous dimension, namely $\gamma_- = 0$ and only γ_+ has to be considered for resummation. The technique used in the case of $n_f = 0$ can be followed to find γ_+ at a resummed level. The complete resummed result is obtained combining γ_+ with the standard NLO unresummed expression of γ_- . A full solution of the evolution equation is then obtained in terms of the two eigenvalues, and projectors $\mathcal{M}_{\pm}(\alpha_s, N)$ on the eigenvectors of the anomalous dimension matrix, as described in the previous section. In Figure (2.8) the resummed splitting function matrix is shown for $n_f = 4$ and $\alpha_s = 0.2$.

Concerning the coefficient functions, the leading small x contributions to partonic cross sections are known to all orders for an increasing number of physical processes. The strategy of resummation is the same used for the splitting functions: double-leading expansion, symmetrization and inclusion of running coupling terms. The resummed results are shown in Figure 2.9.

Combining the ingredients discussed so far, it is possible to determine the resummed predictions for deep-inelastic structure functions, which can then be used also for the determination of PDFs at a resummed level.

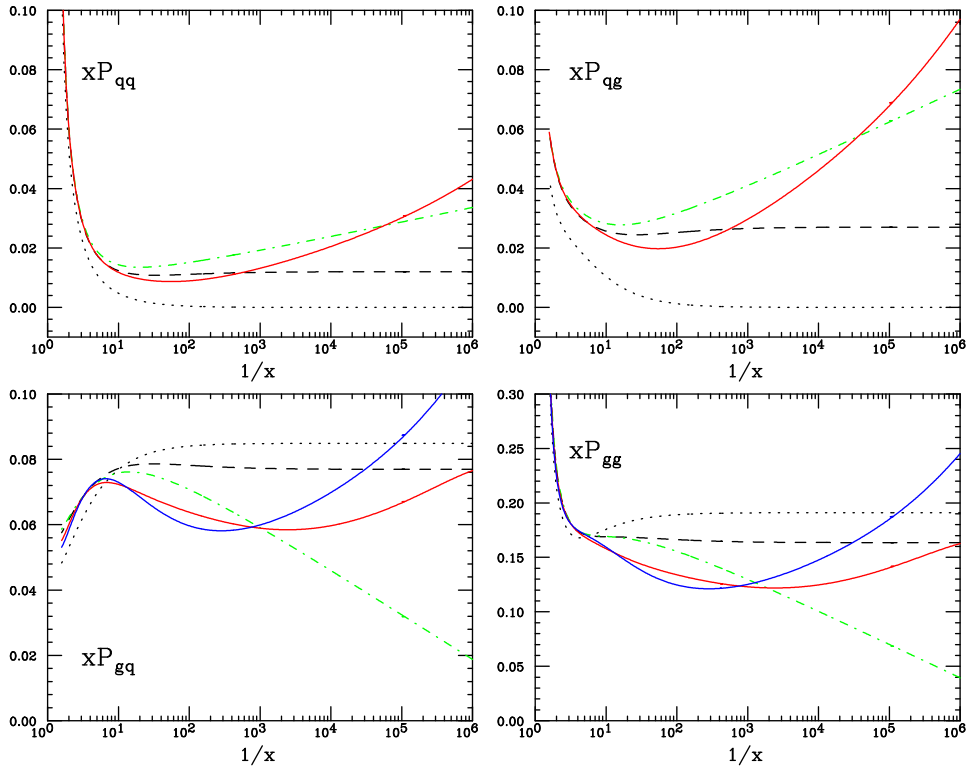


Figure 2.8: Splitting function matrix for $n_f = 4$ and $\alpha_s = 0.2$. The curves correspond to LO (dotted), NLO (dashed), NNLO (dot-dash), resummed (solid)

To estimate the impact of resummation on PDFs, one can take some initial semi-realistic parton densities and then evolve them with the resummed kernels in equation (2.28). In [1], the initial PDFs are taken at $Q_0 = 2\text{GeV}$ and have the following form:

$$xg(x, t_0) = k_g x^{-0.18} (1-x)^5, \quad (2.40)$$

$$xq_v(x, t_0) = k_q x^{0.5} (1-x)^4, \quad (2.41)$$

where k_g and k_q are fixed to satisfy valence and momentum sum rules.

In Figure 2.2.2 the resummed PDFs are shown.

It is evident that the impact of resummation is comparable to that of NNLO corrections, but it goes in the opposite direction, suppressing the initial PDFs.

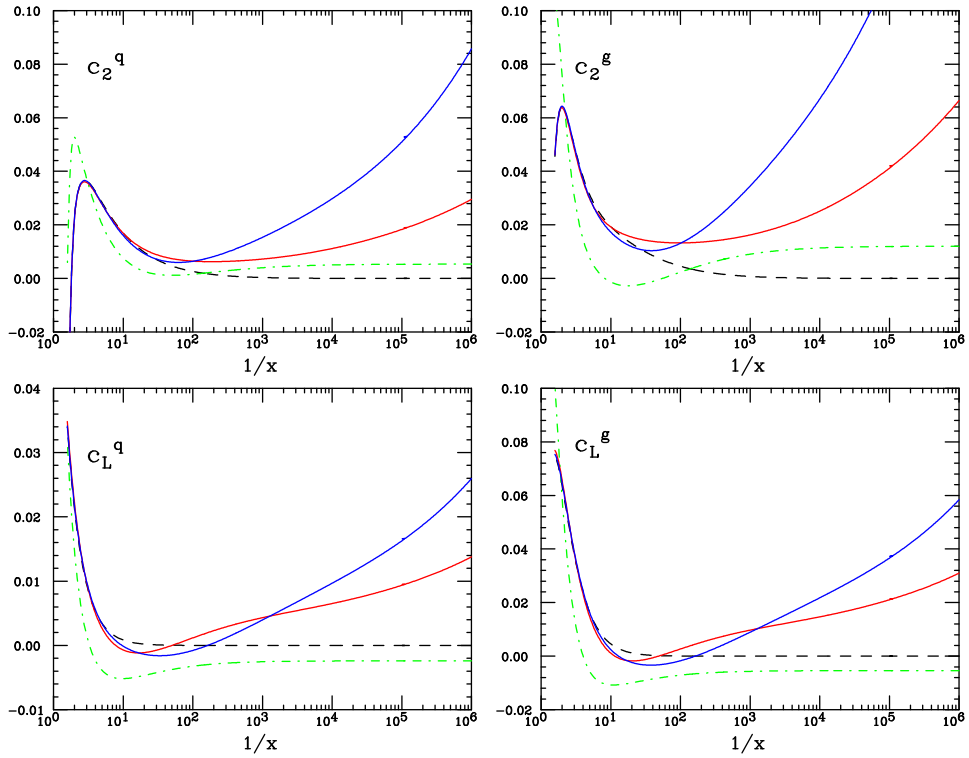


Figure 2.9: Matrix of coefficient functions for $n_f = 4$ and $\alpha_s = 0.2$. The curves correspond to LO (dotted), NLO (dashed), NNLO (dot-dash), resummed (solid)

For future needs, it is important to stress here that the evolution of PDFs is made in Mellin space, where all the convolutions become simple products, and then the x space parton distributions are obtained through Mellin inversion. To follow this procedure an analytic form of PDFs is needed and then it is not possible to implement it in a parton fit.

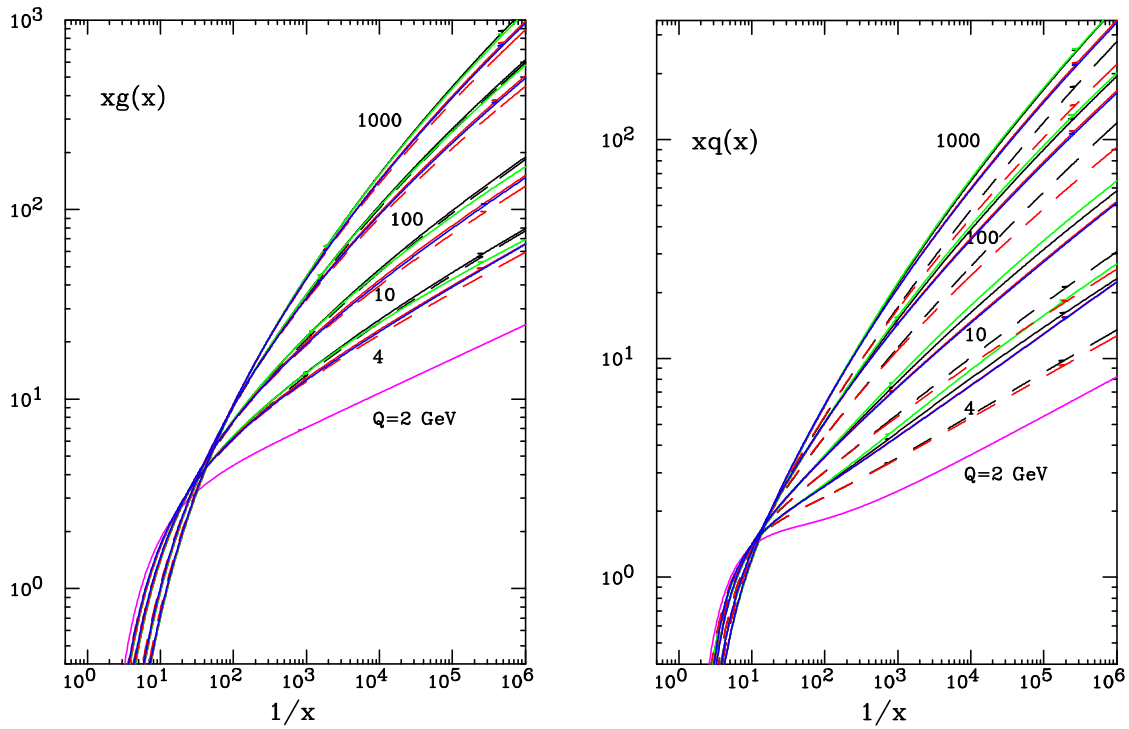


Figure 2.10: The small x behaviour of the gluon distribution (left) and the total (valence plus sea) singlet quark distribution as function of $1/x$ at different values of $Q = 4, 10, 100, 1000$ GeV (for $\alpha_s = 0.2$ and $n_f = 4$). Also shown (purple) the initial parametrization at $Q = 2$ GeV. The curves are: fixed order perturbation theory LO (black dashed), NLO (black solid), NNLO (green); resummed LO (red dashed) and NLO (red solid) in $\overline{\text{MS}}$ scheme resummed NLO (blue solid) in the $\overline{\text{MS}}$ scheme. At all scales, the LO curves are lowest (resummed below fixed order), resummed NLO higher, fixed NLO yet higher and fixed NNLO highest.

Chapter 3

NNPDF approach to the parton fit

The knowledge of Parton Distribution Functions is a crucial aspect for precision physics at hadron colliders, such as the LHC. As already said, PDFs are universal, process-independent, non-perturbative quantities which must be extracted at a given scale from comparison to the available experimental data. They are then evolved by mean of the DGLAP equation to any other scale where they are used as input for theoretical predictions. To reduce the systematic uncertainties in theoretical predictions, a reliable knowledge of PDFs' uncertainties is essential.

At present, there are at least four global sets of parton distributions with uncertainty available and constantly updated by CTEQ-TEA, MRST-MSTW, Alekhin-ABKM and NNPDF groups. The approach of the latter is different from the one of the previous three. In fact, the classical approach is to assume a parametrization based on the functional form $f(x) \sim x^\alpha(1-x)^\beta$ and then tune its parameters to make observables fit experimental data.

The NNPDF collaboration, instead, uses a completely different method. Its aim is to determine objectively both the value and the uncertainty of PDFs from a discrete set of many independent (and possibly incompatible) experimental measure. This goal is reached combining a Monte Carlo method with the use of neural networks as basic interpolating functions. In addition the NNPDF global fit is the only one using consistent NLO QCD.

In this chapter I am going to outline the fundamental features of NNPDF approach, which is summarized in Figure 3.1. In section 3.1, I will present the data which are used to determine PDFs and the Monte Carlo generation of replicas of the original data, then in section 3.2, I will show the fitting strategy using neural networks and in section 3.3, I will describe the FastKernel method to compute the

evolution of PDFs and physical observables. Finally, in section 3.4 I will present the results of the NNPDF approach.

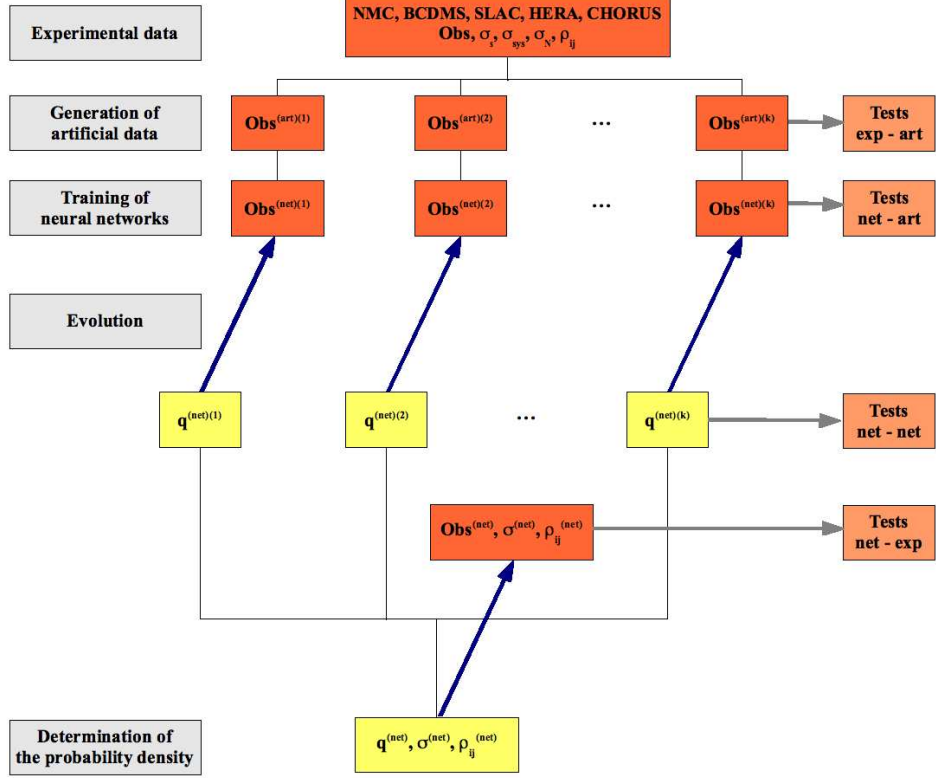


Figure 3.1: Schematic representation of the NNPDF approach [2]

3.1 Experimental data and Monte Carlo generation

The NNPDF2.0 parton determination includes both DIS data and hadronic Tevatron data for fixed-target Drell-Yan, collider weak vector boson and inclusive jet production. The kinematical variables used for the hadronic processes are fully described in [3]. The details of the dataset used are shown in Table 3.1. In Figure 3.2 we can see what is the kinematical region covered by data.

The experimental uncertainties are separated into statistical (including uncorrelated systematics), correlated systematics and normalization uncertainties (see

Deep-Inelastic scattering						
Experiment	Set	N_{dat}	x_{min}	x_{max}	Q_{min}^2 [GeV ²]	Q_{max}^2 [GeV ²]
NMC-pd		260 (153)				
	NMC-pd	260 (153)	0.0015 (0.008)	0.68	0.2 (2.2)	99.0
NMC		288 (245)				
	NMC	288 (245)	0.0035 (0.0056)	0.47	0.8 (2.1)	61.2
SLAC		422 (93)				
	SLACp	211 (47)	0.07	0.85 (0.55)	0.58 (2.0)	29.2
	SLACd	211 (46)	0.07	0.85 (0.55)	0.58 (2.0)	29.1
BCDMS		605 (581)				
	BCDMSp	351 (333)	0.07	0.75	7.5	230.0
	BCDMSd	254 (248)	0.07	0.75	8.8	230.0
HERA1 -AV		741(608)				
	HERA1-NCep	528 (395)	$6.2 \cdot 10^{-7}$ ($3.1 \cdot 10^{-5}$)	0.65	0.045 (2.7)	30000
	HERA1-NCem	145	$1.3 \cdot 10^{-3}$	0.65	90.000	30000
	HERA1-CCep	34	0.008	0.4	300	15000
	HERA1-CCem	34	0.013	0.4	300	30000
CHORUS		1214 (942)				
	CHORUSnu	607 (471)	0.02	0.65	0.3 (2.0)	95.2
	CHORUSnb	607 (471)	0.02	0.65	0.3 (2.0)	95.2
FLH108		8				
	FLH108	8	0.00028	0.0036	12.0	90.000
NTVDMN		90 (84)				
	NTVnuDMN	45 (43)	0.027	0.36	1.1 (2.2)	116.5
	NTVnbDMN	45 (41)	0.021	0.25	0.8 (2.1)	68.3
ZEUS-H2		127				
	Z06NC	90	$5 \cdot 10^{-3}$	0.65	200	310^5
	Z06CC	37	0.015	0.65	280	310^5
Fixed-Target Drell-Yan production						
Experiment	Set	N_{dat}	$[y/x_{min}^F, y/x_{max}^F]$	$[x_{min}, x_{max}]$	M_{min}^2 [GeV ²]	M_{max}^2 [GeV ²]
DYE605		119				
	DYE605	119	[-0.20,0.40]	[0.14,0.65]	50.5	286
DYE866		390				
	DYE866p	184	[0.0,0.78]	[0.017,0.87]	19.8	251.2
	DYE866r	15	[0.05,0.53]	[0.025,0.56]	21.2	166.4
Collider vector boson production						
Experiment	Set	N_{dat}	$[y_{min}, y_{max}]$	$[x_{min}, x_{max}]$	M_{min}^2 [GeV ²]	M_{max}^2 [GeV ²]
CDFWASY		13				
	CDFWASY	13	[0.10,2.63]	$[2.910^{-3}, 0.56]$	6463	6463
CDFZRAP		29				
	CDFZRAP	29	[0.05,2.85]	$[2.9 \cdot 10^{-3}, 0.80]$	8315	8315
D0ZRAP		28				
	D0ZRAP	28	[0.05,2.75]	$[2.9 \cdot 10^{-3}, 0.72]$	8315	8315
Collider inclusive jet production						
Experiment	Set	N_{dat}	$[y_{min}, y_{max}]$	$[x_{min}, x_{max}]$	$p_{T,min}^2$ [GeV ²]	$p_{T,max}^2$ [GeV ²]
CDFR2KT		76				
	CDFR2KT	76	[0.05,1.85]	$[4.6 \cdot 10^{-3}, 0.90]$	3364	3.710^5
D0R2CON		110				
	D0R2CON	110	[0.20,2.2]	$[3.1 \cdot 10^{-3}, 0.097]$	3000	$3.4 \cdot 10^5$
TOTAL						
Experiment	Set	N_{dat}	x_{min}	x_{max}	Q_{min}^2 [GeV ²]	Q_{max}^2 [GeV ²]
TOTAL		4520 (3415)	$3.1 \cdot 10^{-5}$	0.97	2.0	$3.7 \cdot 10^5$

Table 3.1: Experimental datasets included in the NNPDF2.0 global analysis. For DIS experiments we provide in each case the number of data points and the ranges of the kinematical variables before and after (in parenthesis) kinematical cuts. For hadronic data we show the ranges of parton x covered for each set (denoted by $[x_{min}, x_{max}]$), determined using leading order parton kinematics. Note that hadronic data are unaffected by kinematic cuts. The values of x_{min} and Q_{min}^2 for the total dataset hold after imposing kinematic cuts.

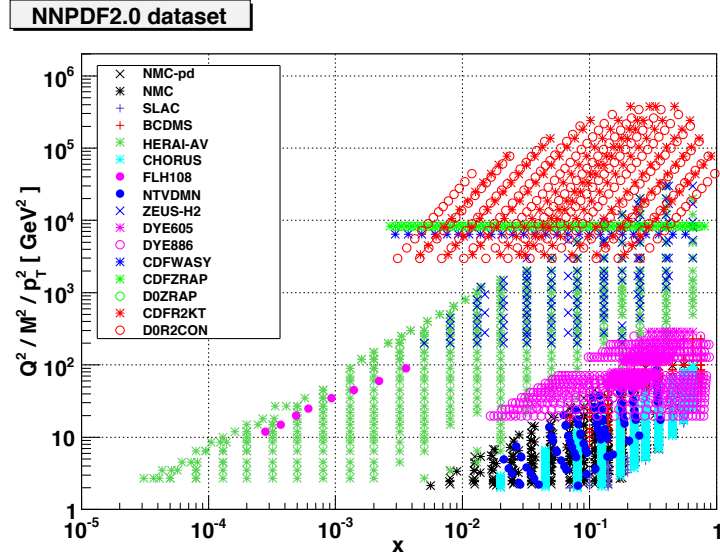


Figure 3.2: Experimental data which enter the NNPDF2.0 analysis (Table 3.1). For hadronic data, the values of x_1 and x_2 , determined by leading order partonic kinematic [3], are plotted (two values per data point).

Table 3.2). From these uncertainties, the covariance matrix can be computed for each dataset as follows:

$$(cov)_{IJ} = \left(\sum_{l=1}^{N_c} \sigma_{I,l} \sigma_{J,l} + \delta_{IJ} \sigma_{I,s}^2 \right) F_I F_J + \left(\sum_{n=1}^{N_a} \sigma_{I,n} \sigma_{J,n} + \sum_{n=1}^{N_r} \sigma_{I,n} \sigma_{J,n} \right) F_I^0 F_J^0, \quad (3.1)$$

where I and J run over the experimental points, F_I and F_J are the measured central values of the observables I and J , N_c is the number of correlated systematic uncertainties, N_a (N_r) is the number of absolute (relative) normalization uncertainties and the index s stands for *statistical*.

Error propagation from experimental data to the fit is handled by a Monte Carlo sampling of the probability distribution defined by data. The statistical sample is obtained generating N_{rep} artificial replicas of data points following the probability distribution of the data. In practice, the data replicas are generated with a multi-gaussian distribution, centered on each data point with the variance given by the experimental uncertainty. The accuracy of the statistical sample is measured through appropriate statistical estimators (this is denoted in Figure 3.1 as "tests exp-art"). From the studies of such quantities, it appears that a Monte Carlo pseudo-data sample with $N_{rep} = 1000$ is sufficient to reproduce the mean values,

Deep-Inelastic scattering				
Set	$\langle\sigma_{stat}\rangle(\%)$	$\langle\text{langle}\sigma_{sys}\rangle(\%)$	$\langle\text{langle}\sigma_{norm}\rangle(\%)$	$\langle\text{langle}\sigma_{tot}\rangle(\%)$
NMC-pd	2.0 (1.7)	0.4 (0.2)	0.0	2.1 (1.8)
NMC	3.7 (3.7)	2.3 (2.1)	2.0	5.0 (4.9)
SLACp	2.7 (3.8)	0.0	2.2	3.6 (4.5)
SLACd	2.5 (3.4)	0.0	1.8	3.1(3.9)
BCDMSp	3.2 (3.1)	2.0 (1.7)	3.2	5.5 (5.2)
BCDMSd	4.5 (4.4)	2.3 (2.1)	3.2	6.6 (6.4)
HERA1-NCep	4.0	1.9 (1.5)	0.5	4.7 (4.5)
HERA1-NCem	10.9	1.9	0.5	11.2
HERA1-CCep	11.2	2.1	0.5	11.4
HERA1-CCem	22.3	3.5	0.5	22.7
CHORUSnu	4.2 (4.1)	6.4 (5.8)	7.9 (7.6)	11.2 (10.6)
CHORUSnb	13.8 (14.9)	7.8 (7.5)	8.7 (8.2)	18.7 (19.1)
FLH108	47.2	53.3	5.0	71.9
NTVnuDMN	16.2 (16.0)	0.0	2.1	16.3 (16.2)
NTVnbDMN	26.6 (26.4)	0.0	2.1	26.7 (26.5)
Z06NC	3.8	3.7	2.6	6.4
Z06CC	25.5	14.3	2.6	31.9
Fixed-target Drell-Yan production				
Set	$\langle\sigma_{stat}\rangle(\%)$	$\langle\text{langle}\sigma_{sys}\rangle(\%)$	$\langle\text{langle}\sigma_{norm}\rangle(\%)$	$\langle\text{langle}\sigma_{tot}\rangle(\%)$
DYE605	16.6	0.0	15.0	22.6
DYE866p	20.4	0.0	6.5	22.1
DYE866r	3.6	1.0	6.1	10.2
Collider vector boson production				
Set	$\langle\sigma_{stat}\rangle(\%)$	$\langle\text{langle}\sigma_{sys}\rangle(\%)$	$\langle\text{langle}\sigma_{norm}\rangle(\%)$	$\langle\text{langle}\sigma_{tot}\rangle(\%)$
CDFWASY	4.2	4.2	0.0	6.0
CDFZRAP	5.1	6.0	6.0	11.5
D0ZRAP	7.6	0.0	6.1	10.2
Collider inclusive jet production				
Set	$\langle\sigma_{stat}\rangle(\%)$	$\langle\text{langle}\sigma_{sys}\rangle(\%)$	$\langle\text{langle}\sigma_{norm}\rangle(\%)$	$\langle\text{langle}\sigma_{tot}\rangle(\%)$
CDFR2KT	4.5	21.1	5.8	23.0
D0R2CON	4.4	14.3	6.1	16.8

Table 3.2: Average statistical, systematic and normalization uncertainties for each of the experimental datasets included in NNPDF2.0. Uncorrelated systematic uncertainties are considered as part of the statistical uncertainty. All uncertainties are given in percentage. For DIS experiments average uncertainties are given both before and (in parenthesis) after cuts.

the variances and the correlations of the experimental data with a 1% accuracy for all the experiments.

3.2 Fitting strategy with neural networks

Once the Monte Carlo replica have been generated, the next step is constructing a set of parton distribution from each replica. Each PDF at a given scale is parametrized by an individual neural network. The choice of neural networks as functional form of parton parametrization is related to the fact that they are very flexible and unbiased, namely they do not introduce a prejudice on the PDFs' functional form. However, it is non trivial determining the best fit form for each replica. Let's go into some details.

The first requirement to obtain the best fit is that it must be independent of any assumption made about the parametrization. This requirement is met by adopting a redundant parametrization, that is the number of parameters used to parametrize the neural networks is much larger than the minimum required in order to reproduce the data. The second issue is to understand what is the right method to determine the best fit. One can think that the answer is obvious and it is found by the minimization of the χ^2 of the comparison between theory and data for a given replica. This method, though, happens to be inadequate, because of the redundancy of the parametrization. In fact it may accommodate not only the smooth shape of the "true" underlying PDFs, but also the random fluctuations of the experimental data about it. The idea then is that the optimal fit should be characterized by a value of χ^2 which is not as small as possible, but rather equal to the value expected on the basis of the fluctuations of the data. The implementation of this idea is based on the cross-validation method. Namely, for each replica, the data are divided randomly into a training set and a validation set. The fit is then performed on the data in the training set, and the χ^2 computed from data in both sets is monitored. Minimization is stopped when the χ^2 in the validation set (not used for fitting) stops decreasing. The method is made possible by the availability of a very large and mostly compatible set of data, and it guarantees that the best fit does not attempt to reproduce random fluctuations of the data. The method also handles incompatible data, by automatically tolerating fluctuations in the data even when they are larger than the nominal uncertainty, whenever fitting these fluctuations would not lead to an improvement of the global quality of the fit. This analysis is denoted as "test net-art" in Figure 3.1, namely, the comparison of neural net to the previously generated artificial data.

After all these steps, we have an ensemble of best fit PDFs, which contains as

many elements as the set of replicas. These can be used to compute physical observables (see Chapter 1) through the *FastKernel* method explained in the next section. Results can be tested for self-consistency (“test net-net” of Figure 3.1): for example one can verify the stability of the results upon a change of parametrization by computing the distance between the results in units of their standard deviations. Also they can be tested for consistency with the data (“test net-exp” of Figure 3.1): namely it is the standard comparison of the final fit prediction with the original input dataset. The most important of these kind of tests is the comparison to the data (and the computation of the corresponding χ^2) for the best fit obtained by averaging results over all neural nets in the final sample.

3.3 FastKernel method

To get the optimal fit, it is necessary to compute physical observables from the parton distribution. As seen in the previous chapters, to perform the calculations of experimental quantities, one needs to convolute the PDF at the appropriate scale (obtained through DGLAP evolution) with the coefficient function of the process. When we have to deal with hadronic colliders observables, a double convolution must be performed.

The method used in the NNPDF approach is called *FastKernel* method and is based on the idea of pre-computing a Green function which takes PDFs from their initial scale to the scale of physical observables. The Green function can be determined in N space, thus requiring a single complex-space integration for the solution of the evolution equation. Furthermore, the Green function can be pre-combined with the hard cross section (coefficient functions) into a suitable kernel, in such a way that the computation of any observable is reduced to the determination of the convolution of this kernel with the pertinent parton distribution, which are parametrized in x space, using neural network, as seen in Section 3.2. The computation of these convolutions is sped up by means of the use of interpolating polynomials.

In the following, I am going to define the most important quantities used to perform the evolution of PDFs (Section 3.3.1) and to compute the DIS observables (Section 3.3.2). I will not go into details of the computation of hadronic observables, because in the next I will focus on DIS. For details about this issue, see [3].

3.3.1 Fast PDF evolution

The PDFs can be written in terms of the following basis:

$$f_j = \{\Sigma, g, V, V_3, V_8, V_{15}, V_{24}, V_{35}, T_3, T_8, T_{15}, T_{24}, T_{35}\}, \quad (3.2)$$

where, Σ excepted, the remaining $2n_f - 1 = 10$ distributions are non-singlet combinations of the quarks' distributions [2].

Provided that Γ_{jk} is the matrix of DGLAP evolution (see equation (1.51)), the PDFs evolved from the initial scale Q_0^2 to the scale of the experimental point I can be written as:

$$f_j(x_I, Q_I^2) = \sum_{k=1}^{N_{pdf}} \int_{x_I}^1 \frac{dy}{y} \Gamma_{jk} \left(\frac{x_I}{y}, Q_0^2, Q_I^2 \right) f_k(y, Q_0^2). \quad (3.3)$$

To perform numerically the integral, we need first to define a grid in x (independent from the value of x_I) with N_x points, such that:

$$x_{min} = x_1 < x_2 < \dots < x_{N_x-1} < x_{N_x} = 1, \quad (3.4)$$

then we introduce a set of interpolating functions \mathcal{I}^α with the following properties:

$$\mathcal{I}^\alpha(x_\alpha) = 1 \quad (3.5)$$

$$\mathcal{I}^\alpha(x_\beta) = 0, \quad \beta \neq \alpha \quad (3.6)$$

$$\sum_{\alpha=1}^{N_x} \mathcal{I}^\alpha(y) = 1, \quad \forall y. \quad (3.7)$$

With these tools, the PDFs at the initial scale can be approximated as

$$f_k^0(y) = \sum_{\alpha=1}^{N_x} f_k^0(x_\alpha) \mathcal{I}^\alpha(y) + \mathcal{O}[(x_{\alpha+1}x_\alpha)^p], \quad (3.8)$$

where p is the lowest order neglected in the interpolation. Hence, equation (3.3) becomes:

$$\begin{aligned} f_j(x_I) &= \sum_{k=1}^{N_{pdf}} \sum_{\alpha=1}^{N_x} f_k^0(x_\alpha) \int_{x_I}^1 \frac{dy}{y} \Gamma_{jk} \left(\frac{x_I}{y} \right) \mathcal{I}^\alpha(y) + \mathcal{O}[(x_{\alpha+1} - x_\alpha)^p] = \\ &= \sum_{k=1}^{N_{pdf}} \sum_{\alpha=1}^{N_x} \hat{\sigma}_{\alpha k}^{Ij} f_k^0(x_\alpha) + \mathcal{O}[(x_{\alpha+1} - x_\alpha)^p], \end{aligned} \quad (3.9)$$

where

$$\hat{\sigma}_{\alpha k}^{Ij} = \hat{\sigma}_{\alpha k}^{Ij}(x_I, Q_0^2, Q_I^2) = \int_{x_I}^1 \frac{dy}{y} \Gamma_{jk} \left(\frac{x_I}{y} \right) \mathcal{I}^\alpha(y). \quad (3.10)$$

Having precomputed the $\hat{\sigma}_{\alpha k}^{Ij}$ coefficients for each experimental point I , the evolution of PDFs only require N_x evaluation of the PDFs at the initial scale, independent of the point at which the evolved PDFs are needed, thereby reducing the computational cost of evolution. The choice of the interpolant functions is crucial, because with an appropriate basis better accuracy can be obtained with a smaller number of points, reducing computational cost.

3.3.2 Fast computation of DIS observables

Using the strategy described in the previous section, we can easily write down the expressions for the DIS observables included in our fit. The factorized expression for physical quantities is (see section (1.2.1)):

$$\sigma_I^{DIS}(x_I, Q_I^2) = \sum_{k=1}^{N_{pdf}} C_{Ik} \otimes f_k(x_I, Q_I^2) = \sum_{k=1}^{N_x} \int_{x_I}^1 \frac{dy}{y} C_{Ik} \left(\frac{x_I}{y}, \alpha_s(Q_I^2) \right) f_k(y, Q_I^2), \quad (3.11)$$

where I denotes both the observable and the kinematic point. Now, we can absorb the coefficient C_{Ik} into a modified kernel K_{Ij} which can be precomputed before starting the fit:

$$K_{Ij}(x_I, \alpha_s(Q_I^2), \alpha_s(Q_0^2)) = \sum_{k=1}^{N_{pdf}} C_{Ik} \otimes \Gamma_{kj}(x_I, \alpha_s(Q_I^2), \alpha_s(Q_0^2)). \quad (3.12)$$

The kernel acts on the j -th PDFs at the initial scale and it is an observable-dependent linear combination of products of coefficient functions and evolution kernels. If we substitute equations (3.9) and (3.12) into (3.11), we get the expression of the observable I using the interpolant functions \mathcal{I}^α

$$\begin{aligned} \sigma_I^{DIS}(x_I, Q_I^2) &= \sum_{k=1}^{N_{pdf}} \sum_{\alpha=1}^{N_x} f_j^0(x_\alpha) \int_{x_I}^1 \frac{dy}{y} K_{Ij} \left(\frac{x_I}{y} \right) \mathcal{I}^\alpha(y) = \\ &= \sum_{k=1}^{N_{pdf}} \sum_{\alpha=1}^{N_x} \hat{\sigma}_{\alpha j}^I f_k^0 + \mathcal{O}[(x_{\alpha+1} - x_\alpha)^p], \end{aligned} \quad (3.13)$$

where

$$\hat{\sigma}_{\alpha j}^I = \hat{\sigma}_{\alpha j}^I(x_I, Q_0^2, Q_I^2) = \int_{x_I}^1 \frac{dy}{y} K_{Ij} \left(\frac{x_I}{y} \right) \mathcal{I}^\alpha(y). \quad (3.14)$$

In the case of hadronic observables, the strategy is different: instead of including the coefficient function into the kernel according to equation (3.12), we compute the convolution (3.11) using the fast interpolation method.

3.4 Results

In this section I will present the PDFs set obtained by NNPDF collaboration as shown in [3].

The global fit is performed with three active flavours (u , d , s) and the gluon. In Figures 3.3 and 3.4 the quarks and gluon distributions and their uncertainties at the initial scale $Q_0^2 = 2\text{GeV}^2$ are displayed, compared with the results of the CTEQ-TEA and MRST-MSTW collaborations. The uncertainties of NNPDF2.0 are over all comparable to CTEQ6.6 and MSTW08 ones. The exceptions are interesting, because they seem to be related to the number of parameters of the parametrization used for the parton fit. In fact, the uncertainty on strangeness, which NNPDF2.0 parametrizes with as many parameters as any other PDF, is rather larger than those of MSTW08 and CTEQ6.6, in which these PDFs are parametrized with a very small number of parameters. The NNPDF2.0 uncertainty on total quark singlet (which contains a sizable strange contribution) is also larger. The uncertainty on the small x gluon is significantly larger than that found by CTEQ6.6, but comparable to that MSTW08, which has an extra parameter to describe the small x gluon in comparison to CTEQ6.6.

On the other side, in the triplet case, the NNPDF uncertainty is smaller than that of the other two groups. The triplet distribution is strongly constraint by data and the smaller uncertainties of the NNPDFs suggests that the "tolerance" parameter, introduced by CTEQ and MRST-MSTV groups to include in the global fit a large variety of different data (possibly incompatible), brings to overestimate the actual uncertainties of PDFs.

The uncertainty bands shown are one-sigma, and not 68% confidence level. The comparison between these two bands is shown in Figure 3.5 and it allows checking if there is a significant departure from gaussian behavior of the fitted PDFs. In the regions in which the PDFs are constrained by experimental data, the standard deviation and the 68% confidence levels coincide to good approximation, thus suggesting gaussian behavior. However, in the extrapolation region for most PDFs deviations from gaussian behavior are sizable. This is especially noticeable for the gluon at small x , and for the quark singlet and total strangeness both at small and large x . The small x behavior could be better understood thanks to the LHC data, where the kinematical range is pushed down to $x \sim 10^{-6} - 10^{-7}$. It could

be then crucial to perform a parton fit including the LL x theoretical corrections. The latter is exactly the aim of the present work and in the next chapter I will show the progress in the implementation of small x resummation in the NNPDF code.

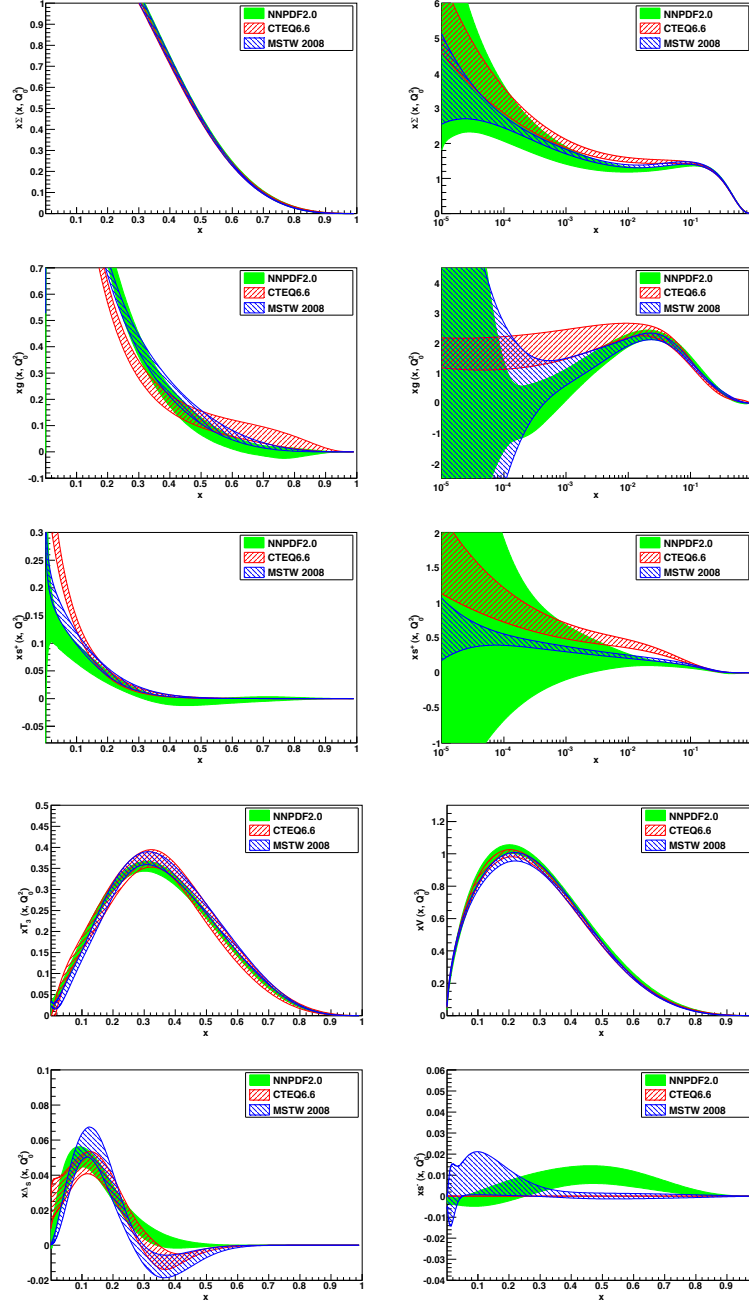


Figure 3.3: The singlet $\Sigma(x)$, gluon $g(x)$, total strangeness $s^+(x)$ (both on logarithmic (left) and linear (right) scale), triplet $T_3(x)$, total valence $V(x)$, sea asymmetry $\Delta S(x)$ and strangeness asymmetry $s_-(x)$ (on linear scale), at the initial scale $Q_0^2 = 2\text{GeV}^2$ from the NNPDF2.0 analysis compared to MSTW08 and CTEQ6.6 PDFs.

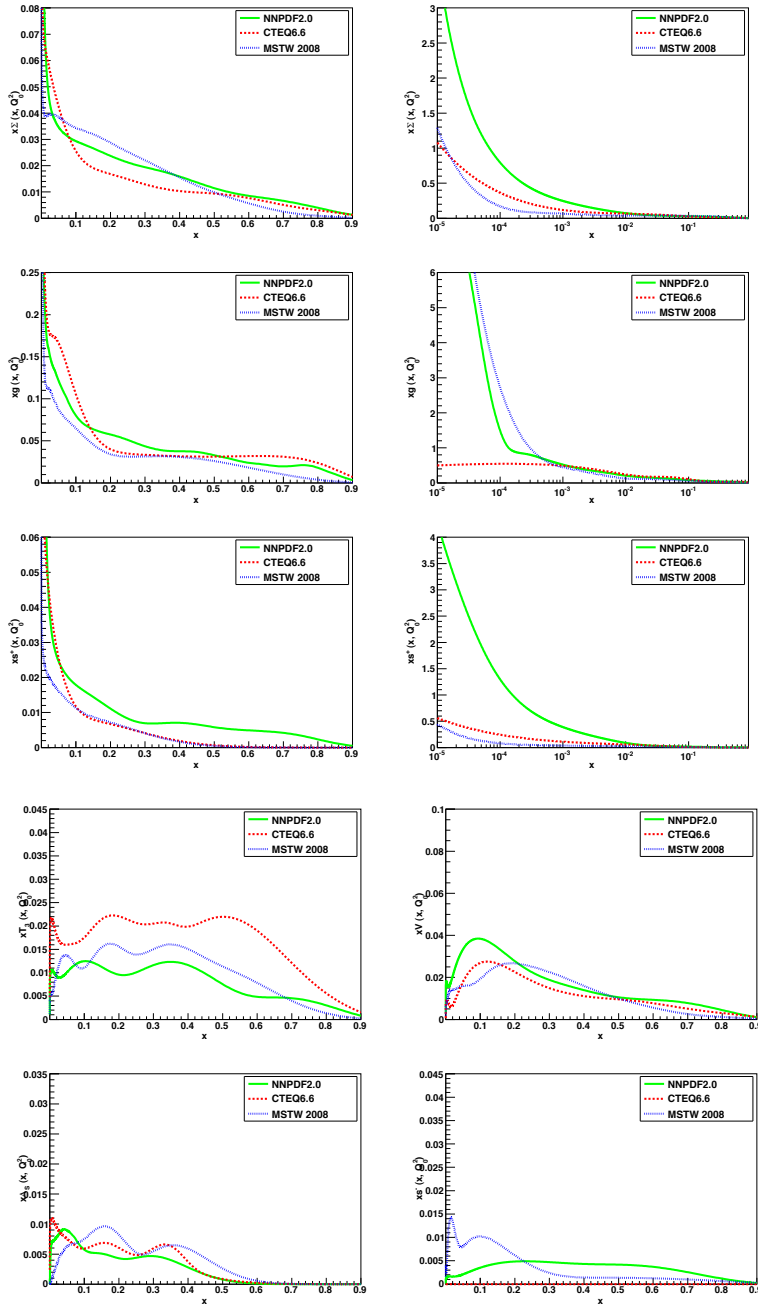


Figure 3.4: The uncertainties of singlet $\Sigma(x)$, gluon $g(x)$, total strangeness $s^+(x)$ (both on logarithmic (left) and linear (right) scale), triplet $T_3(x)$, total valence $V(x)$, sea asymmetry $\Delta S(x)$ and strangeness asymmetry $s_-(x)$ (on linear scale), at the initial scale $Q_0^2 = 2\text{GeV}^2$ from the NNPDF2.0 analysis compared to MSTW08 and CTEQ6.6 PDFs.

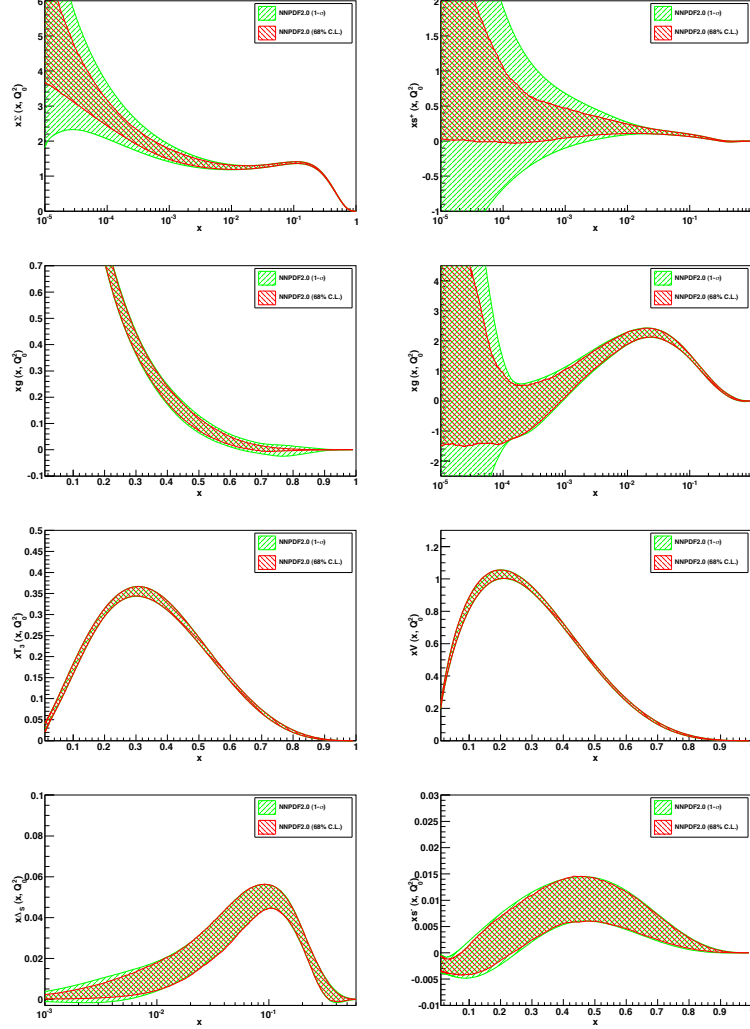


Figure 3.5: The uncertainties of singlet $\Sigma(x)$, gluon $g(x)$, total strangeness $s^+(x)$ (both on logarithmic (left) and linear (right) scale), triplet $T_3(x)$, total valence $V(x)$, sea asymmetry $\Delta S(x)$ and strangeness asymmetry $s_-(x)$ (on linear scale), at the initial scale $Q_0^2 = 2\text{GeV}^2$ from the NNPDF2.0 analysis compared to MSTW08 and CTEQ6.6 PDFs.

Chapter 4

Implementation of small x resummation in the NNPDF code

To get a small x global parton fit, one needs to perform at LLx accuracy both the evolution of PDFs and the computation of hard cross-sections. In the context of NNPDF, as outlined in the previous chapter, the computation of the evolution kernels and of the coefficient functions is carried out through the FastKernel method, with the use of Mellin space techniques. So the crucial issue is enabling the FastKernel code to compute physical observables at LLx accuracy.

In this chapter I will present the progress in the implementation of small x resummed results, as computed in the ABF approach [1], in the FastKernel code. In section 4.1, I will remark some crucial aspects of the small x resummed results, which make their inclusion in a parton fit non trivial . Then, in section 4.2, I will outline the strategy I followed to actually implement small x resummation in the FastKernel code. Finally, in section 3.4, I will show and discuss the results I obtained.

4.1 Preliminary studies

As outlined in Section 2.1.2, the solution of DGLAP equation at LLx accuracy needs to be found through the path-integral method, because the resummed quantities include all orders in α_s . Thus, before adding the small x resummation, one has to check that the NLO truncated solution coincides with the NLO solution obtained with the path-integral, in order to be sure that the implementation of the new method is correct. Hence, I performed the calculation of the evolution of the gluon distribution from 2 GeV to 100 GeV using the two methods and then I

computed the the ratio between the two results, which is expected to be equal to one. In fact I obtained one within the 1% of accuracy.

Now, we can turn to the disamine of some features of resummed results, keeping in mind that we want to use their Mellin transform (as defined in equation (1.33)) to compute the evolution kernels (1.51) and (3.12), come back to x space and perform the computation of observables as outlined in section 3.3.

In Chapter 2, we saw that resummed anomalous dimension can be expressed in terms of Bateman functions. Its analytic form, then, is not suitable for our purpose, because it would involve a strong increase in the computational cost of the global parton fit. For this reason we cannot follow the ABF strategy to implement the small x resummed quantities in the NNPDF code. We need to compute them in a more convenient way.

First of all, the quantities needed for the resummation of physical observables, like the structure functions $F_2(x, Q^2)$ and $F_L(x, Q^2)$, are defined in Table 4.1. Now, the

Notation	Definition
P_{gg}	Gluon-gluon splitting function
P_{gq}	Gluon-quark splitting function
P_{qg}	Quark-gluon splitting function
P_{qq}	Quark-quark splitting function
C_2^q	Quark coefficient function for \overline{F}_2
C_2^g	Gluon coefficient function for \overline{F}_2
C_L^q	Quark coefficient function for F_L
C_L^g	Gluon coefficient function for F_L

Table 4.1: Definition of the quantities needed for resummation of physical observables

approach we use in this work to compute them is numerical and can be outlined as follows.

1. Using analytic expression from [1] of ABF, we extract the $Q_0\overline{\text{MS}}$ resummed correction Δ_{res} , namely the difference between the NLO computation and NLO $Q_0\overline{\text{MS}}$ resummed result, for each of the quantities listed in Table 4.1. To do this we define a grid of x values with 600 points evenly spaced in $\text{Log}(x)$, from one down to 10^{-6} . From this grid we can define the points (x, Δ_{res}) of the interpolation of small x resummed correction, where $\Delta_{res} = x \cdot (P_{NLO} - P_{res})$. Such interpolation is built for 57 values of α_s , from 0.08 to 0.36.

2. The next step is finding an adequate parametrization for the interpolations of resummed corrections. The requirement that our choice must meet is that the functions we use to build up the parametrization must have an analytic Mellin transform. In this way, once we have found the best coefficients to fit our starting form with the chosen parametrization, we have the Mellin transform of Δ_{res} , without having to compute any integral.
3. Once the parametrization have been chosen, for each value of α_s , we fit the interpolation of Δ_{res} with it and store the coefficients.

After these three steps, we obtain an expression for the resummed corrections of the quantities of Table 4.1 that can be implemented in the FastKernel code, as I will show in the next section.

Now, let us go into some details of the parametrizations, which we based on two different functional forms: one for all the splitting functions and one for all the coefficient functions. The features the parametrization has to match are the following:

1. it must reproduce with optimal accuracy the x space form of the quantities in Table 4.1.
2. its Mellin transform must not have singularities which can affect the numerical Mellin inversion to be performed within the FastKernel code to compute physical observables. One has to pay attention about this issue in particular in the case of splitting functions, because, in order to compute the evolution kernels, they will be used as exponents.

To find the best parametrization which satisfies the above conditions, I studied different combinations of logarithms and powers of x .

For both splitting functions and coefficient functions I started with a series of $\text{Log}\frac{1}{x}$. I found that such a parametrization fits quite accurately the data in x space with $N_{coeff} = 11$ and its Mellin inversion can be computed numerically, but it introduces in N space a pole in zero of order $k = 12$. For this reason I used it only for the coefficient functions, as shown in the following discussion. Concerning the splitting functions, before selecting the parametrization I will show in the next section, I tried other different functional forms, which I enumerate describing their properties and problems.

1. $\sum_{i=0}^{N_{coeff}} c_i x^i$: it has a not good fit accuracy in x space, but its Mellin transform is adequate for our purpose (it has N_{coeff} simple pole in the real negative axis).

2. $\frac{k}{x^{c \cdot \alpha_s}} + \sum_{i=0}^4 + \text{Log}\left(\frac{1}{x}\right)$: it does not have the same fit accuracy for all the values of α_s and for all the splitting functions. Its Mellin transform is adequate for our purpose.
3. $\frac{k}{x^{c \cdot \alpha_s}}(1-x)^a (c_0 + c_1 x^{1/4} + c_2 x^{1/8} + c_3 x^{1/16})$: it has an optimal fit accuracy, but its Mellin transform presents spurious singularities.

4.1.1 Splitting functions

Before describing the chosen parametrization for the splitting functions, I show in Figures 4.1 and 4.2 the form of the resummed corrections ΔP_{gg}^{res} , ΔP_{gq}^{res} , ΔP_{qq}^{res} , for three different values of α_s (0.08, 0.25, 0.36) and $n_f = 4$. From the plots it is evident that all the resummed corrections show a faster rise at small x as α_s increases. This issue is to be related to the dependence on α_s of the position of singularity in the resummed results, shown in Figure 2.5. ΔP_{gg} and ΔP_{gq} show a dip for values of x smaller than 0.1 and a subsequent rise at very small values of x . The absolute scale of ΔP_{gq} is smaller than the one of ΔP_{gg} , because of the ratio of color Casimir factors $\frac{C_F}{C_A}$. In the case of ΔP_{qq} and ΔP_{gq} of Figure 4.2 the rise begins at smaller values of x and the dip is barely visible increasing values of α_s .

The resummed correction is only included for values greater of x greater than 0.5.

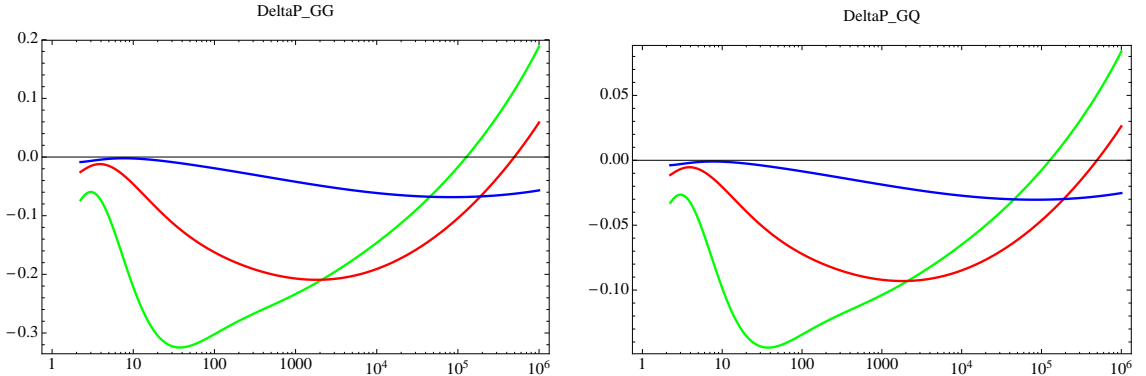


Figure 4.1: ΔP_{gg}^{res} (left) and ΔP_{gq}^{res} (right) for $n_f = 4$ and $\alpha_s = 0.08$ (blue), 0.2 (red), 0.36 (green).

Now, let us turn to the description of the chosen parametrization, which encloses the good properties of the different functional forms listed in the introduction to this section and avoids their problems.

In Chapter 2, we saw that the resummed anomalous dimensions develop a singularity, whose position is related to the value of α_s . The nature of this sin-

gularity happens to be a simple pole. To account for this well-known analytic behavior of the resummed anomalous dimensions at small x , we have to put in our parametrization in x space a function whose Mellin transform presents a simple pole in $N = c \cdot \alpha_s$, where c is an appropriate coefficient, namely

$$f_1(x) = \left(\frac{1}{x}\right)^{c \cdot \alpha_s} \rightarrow \mathcal{M}[f_1(x)](N) = \frac{1}{N - c \cdot \alpha_s}. \quad (4.1)$$

It should be notice that the function 4.1 describes the behavior of the splitting function when $x \rightarrow 0$. Our interpolations stop at $x = 10^{-6}$, that is a value not so small to be considered actually in the asymptotic region. Then the behavior of the correction at small x is not exactly described by 4.1. In addition, we need to reproduce the splitting functions in the whole region of x covered by the interpolation. The parametrization I use is the following:

$$k \cdot \frac{1}{x^{c \cdot \alpha_s}} + c_0 + \sum_{i=1}^5 c_i x^i + c_6 \cdot \text{Log}\left(\frac{1}{x}\right) + c_7 \cdot \text{Log}\left(\frac{1}{x}\right)^2 + c_8 \cdot \text{Log}\left(\frac{1}{x}\right)^3. \quad (4.2)$$

The Mellin transform of (4.2) is

$$k \cdot \frac{1}{N - c \cdot \alpha_s} + \frac{c_0}{N} + \sum_{i=1}^5 \frac{c_i}{N + i} + \frac{c_6}{N^2} + \frac{c_7}{N^3} + \frac{c_8}{N^4} \quad (4.3)$$

and it has the property we need. In fact the rightmost singularity is the one in $c \cdot \alpha_s$ and it determines the small x behavior of resummed solution to DGLAP equation. The other singularities are to left.

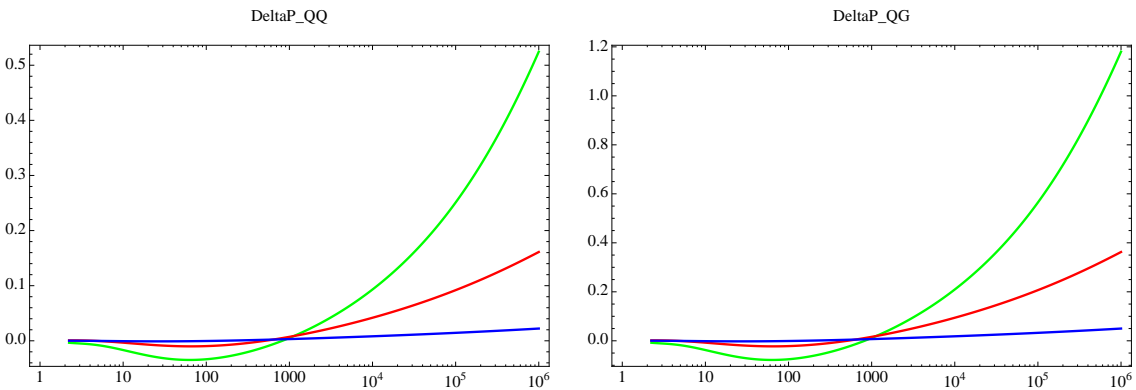


Figure 4.2: ΔP_{qq}^{res} (left) and ΔP_{qg}^{res} (right) for $n_f = 4$ and $\alpha_s = 0.08$ (blue), 0.2 (red), 0.36 (green).

The next step is fitting the interpolations (x, Δ_{res}) with the chosen parametrization. In Figures 4.3 and 4.4, I show the original data compared to the fitted curve for $\alpha_s = 0.2$. To measure the quality of the fit I defined the relative accuracy σ_{rel}

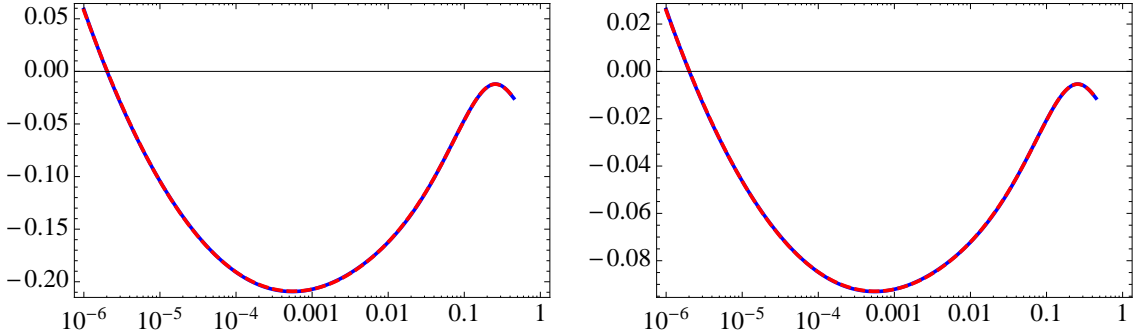


Figure 4.3: ΔP_{gg}^{res} (left) and ΔP_{gq}^{res} (right) for $n_f = 4$ and $\alpha_s = 0.2$. The interpolation form (blue) and the fit (red, dashed) are shown.

as:

$$\sigma_{rel}(x) = \frac{|\Delta_{res}(x) - \Delta_{res}^{Fit}(x)|}{\Delta_{res}(x)}, \quad (4.4)$$

where $\Delta_{res}^{Fit}(x)$ is the fit functional form computed as a function of x . In Figures 4.5 and 4.6 the distribution of $\sigma_{rel}(x)$ is shown, for the plots of Figures 4.3 and 4.4. We can see that the relative accuracy is below 5% in almost the whole x range. The points in which $\sigma_{rel}(x)$ is largest are the points where $\Delta_{res}(x)$ is zero.

For the other values of α_s the agreement between interpolations and fit is almost the same. The coefficients of the fit are stored in four files (one for each splitting function), following the order of increasing α_s .

4.1.2 Coefficient functions

Before going into the details of the chosen parametrization for the coefficient functions, I show in Figures 4.7 and 4.8 the form of the small x resummed corrections $\Delta C_2^g, \Delta C_2^q, \Delta C_L^g, \Delta C_L^q$, for three different values of α_s (0.08, 0.25, 0.36) and $n_f = 4$.

The parametrization I used is:

$$c_0 + \sum_{i=1}^{11} c_i \left[\text{Log} \left(\frac{1}{x} \right) \right]^i. \quad (4.5)$$

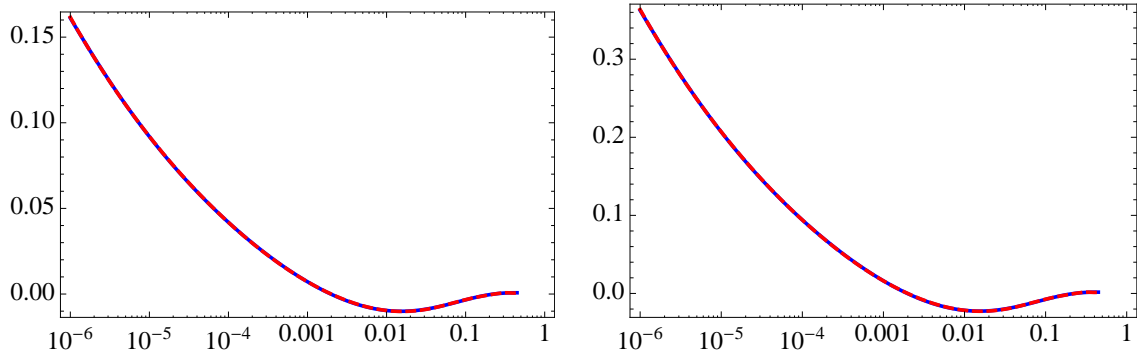


Figure 4.4: ΔP_{qq}^{res} (left) and ΔP_{qq}^{res} (right) for $n_f = 4$ and $\alpha_s = 0.2$. The interpolation form (blue) and the fit (red, dashed) are shown.

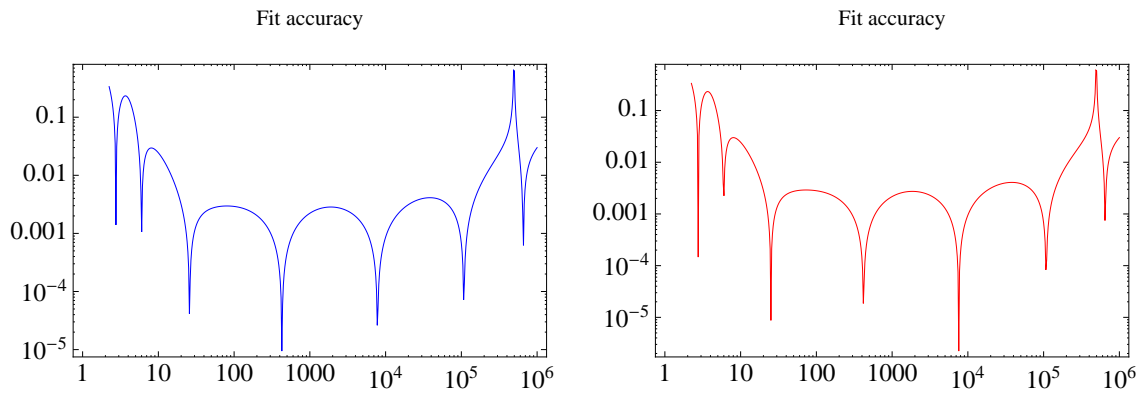


Figure 4.5: Fit accuracy for P_{gg} (left) and P_{gq} (right) for $n_f = 4$ and $\alpha_s = 0.2$.

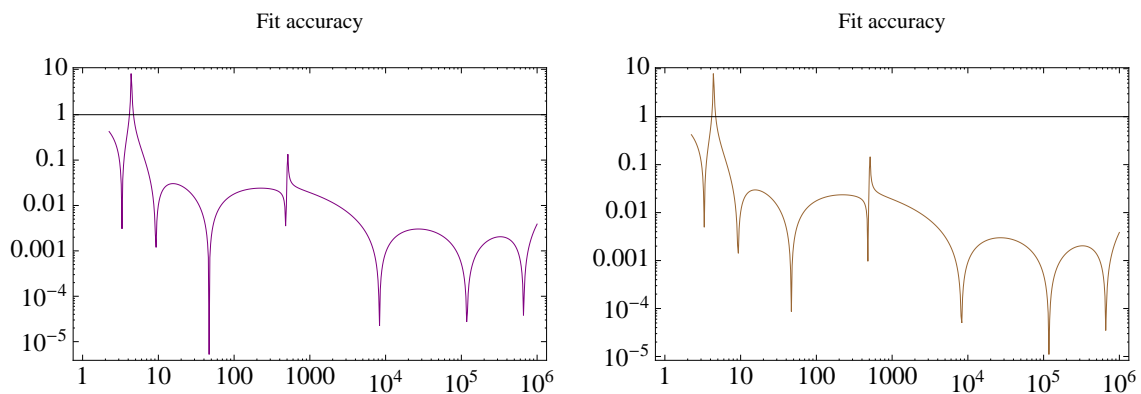


Figure 4.6: Fit accuracy of P_{qq} (left) and P_{qg} (right) for $n_f = 4$ and $\alpha_s = 0.2$.

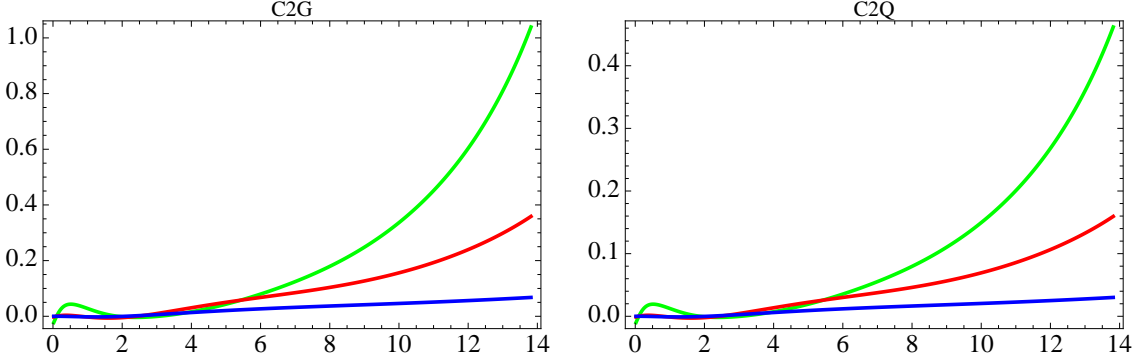


Figure 4.7: ΔC_2^g (left) and ΔC_2^q (right) for $n_f = 4$ and $\alpha_s = 0.08$ (blue), 0.2 (red), 0.36 (green).

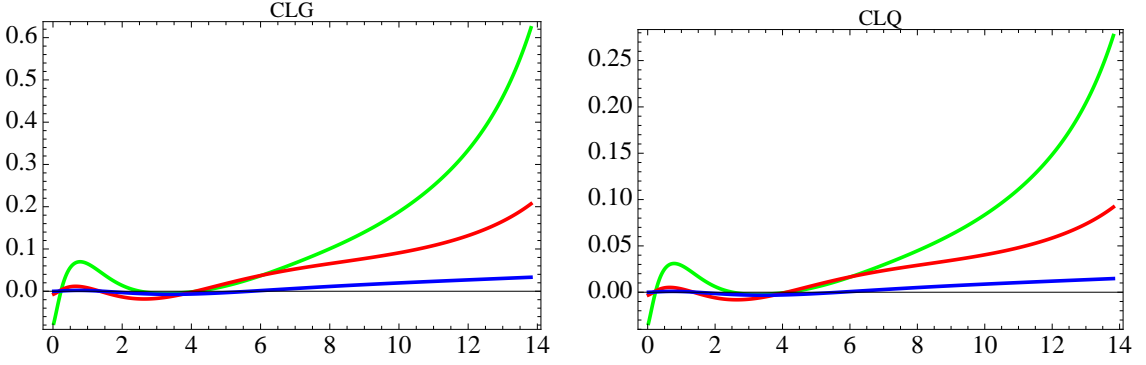


Figure 4.8: ΔC_L^g (left) and ΔC_L^q (right) for $n_f = 4$ and $\alpha_s = 0.08$ (blue), 0.2 (red), 0.36 (green).

Also in this case the Mellin transform of (4.5) is well-known:

$$\sum_{i=1}^{12} \Gamma(i) \frac{c_i}{N^i}. \quad (4.6)$$

Now, we come to the fit. In Figures 4.9 and 4.10, I show the original data compared to the fitted curve for $\alpha_s = 0.2$. In Figures 4.11 and 4.12, the distribution of the relative accuracy $\sigma_{rel}(x)$ (equation (4.4)) is shown, for the plots of Figures 4.9 and 4.10. From the plots we can see that the relative accuracy is below 0.1% in almost the whole x range. Hence the agreement between fit and interpolation is very good. The coefficients of the fit are stored in four files (one for each coefficient function), following the order of increasing α_s .

4.2 Implementation of small x resummation in the FastKernel code

To implement the small x resummation, as already discussed, I have modified the code of the FastKernel method, adding two subroutines (one for the splitting functions and one for the coefficient functions) to make the computation of the needed quantities at LL x accuracy possible.

First, in Section 4.2.1, I briefly introduce the structure of the *Fortran* code. Then I explain the logic of the implementation, in Section 4.2.2. Finally the checks of the correctness of the implementation are presented in Section 4.2.3.

4.2.1 Structure of FastKernel code

The basic ideas of the FastKernel method have been already outlined in Section 3.3. Now, I want to give some details about the procedure followed by the code to actually perform the calculation, to understand where the small x resummation option must be included.

In order to decide at what accuracy the calculation must be performed, the character variable PTORD, i.e. perturbative order, is defined in the code. The first thing to do is then adding the small x option within the possible assignments of PTORD. Depending on the PTORD value, then, the code assigns to some dedicated variables (the integer IPT and the logical RESUM_SMX) a different value. The possible assignments of PTORD and the related values of IPT and RESUM_SMX are reported in Table 4.2.

Once the perturbative order is decided, the next step is selecting the method to perturbatively solve the DGLAP equation at the accuracy level assigned. The

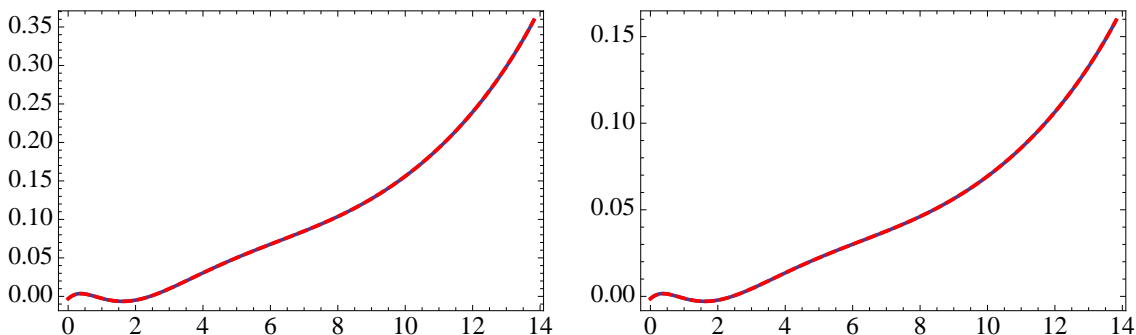


Figure 4.9: ΔC_2^g (left) and ΔC_2^g (right) for $n_f = 4$ and $\alpha_s = 0.2$. The interpolation form (blue) and the fit (red, dashed) are shown.

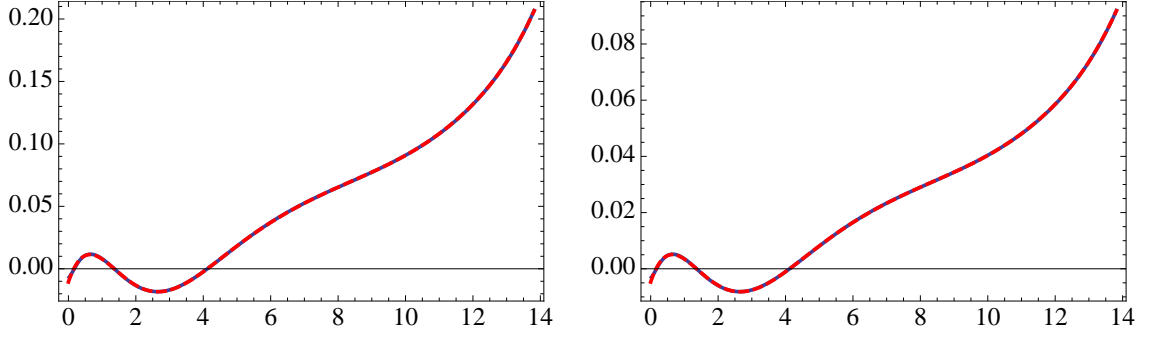


Figure 4.10: ΔC_L^g (left) and ΔC_L^q (right) for $n_f = 4$ and $\alpha_s = 0.2$. The interpolation form (blue) and the fit (red, dashed) are shown.

Fixed Order - Unpolarized evolution			
PTORD	Perturbative Order	IPT	RESUM.SMX
"N0LO_FXD_UNP"	LO	0	false
"N1LO_FXD_UNP"	NLO	1	false
"N2LO_FXD_UNP"	NNLO	2	false
Small x resummation			
PTORD	Perturbative Order	IPT	RESUM.SMX
"N0LO_RES_SMX"	LO + LL x	0	true
"N1LO_RES_SMX"	NLO + LL x	1	true
"N2LO_RES_SMX"	NNLO + LL x	2	true

Table 4.2: The possible assignments of PTORD and the related values of IPT and RESUM.SMX

dedicated variable is MODEV and, depending on its value, a different number is assigned to IMODEV, as shown in Table 4.3. As already stressed, the inclusion of

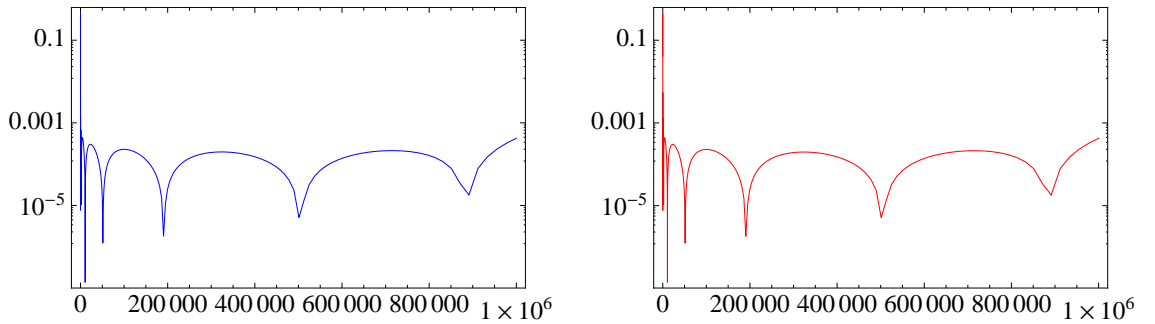


Figure 4.11: Fit accuracy of ΔC_2^g (left) and ΔC_2^q (right) for $n_f = 4$ and $\alpha_s = 0.2$.

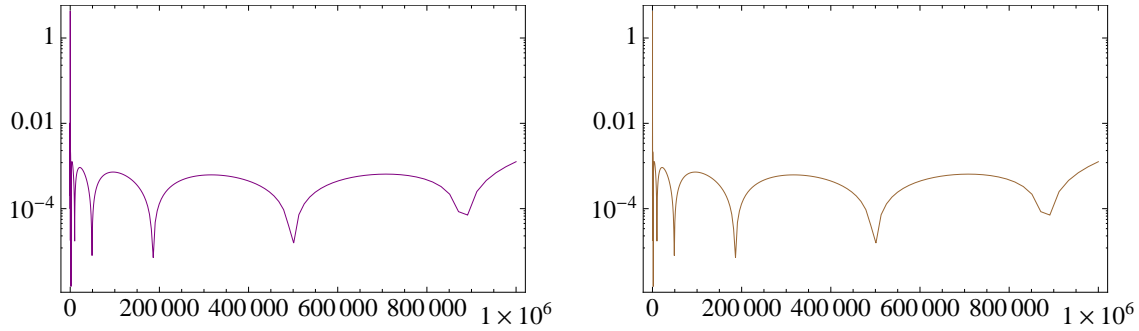


Figure 4.12: Fit accuracy of ΔC_L^g (left) and ΔC_L^q (right) for $n_f = 4$ and $\alpha_s = 0.2$.

small x resummed results implies the use of the path-integral numerical method. Obviously, the value of both PTORD and MODEV can be given as input by the user, together with the value of the scale Q^2 of the physical observables.

MODEV	Method to solve DGLAP	IMODEV
"TRN"	Fully truncated solution	0
"ITE"	Iterated solution	1
"PTH"	Path-integral numerical solution	2

Table 4.3: The possible assignments of MODEV and the related values of IMODEV

After the inclusion of small x option in the assignments of PTORD and of the path-integral option in the assignments of MODEV, small x resummation of physical observables can actually be activated. Let us see where the computation of resummed correction must be included.

We have already said that the computation of the evolution kernels is performed in Mellin space, where all the convolutions become simple products. Then one need to have the Mellin transform expression of the splitting function matrix and of the coefficient functions at LL x accuracy. To get them I added the small x resummation option to the routines that compute anomalous dimensions and coefficient functions at fixed order level. If RESUM_SMX has the assignment "true", then the code accesses to the small x resummed calculation, which is described in the next section.

4.2.2 Logics of the Fortran implementation

In preliminary studies, I have found the parametrizations (4.2) and (4.5) to describe the small x resummed corrections to the splitting function matrix and to

the coefficient functions, respectively. Then, the idea of the Fortran implementation of small x resummation is simply to add these contributions to the already implemented fixed order results. To actually put in practice this simple idea, there are some tricky issues to solve, related to the value of α_s .

In the code, the value of $\alpha_s(Q^2)$ is determined solving numerically the renormalization group equation (1.8). Hence, α_s can assume a continuous number of values.

At the level of a perturbative fixed order calculation, the splitting functions and the anomalous dimensions are computed using their analytic expressions, which contain a well-defined dependence on α_s and then vary continuously with it. At a small x resummed level, we use the numerical method explained in Section 4.1, which provides, on the contrary, an expression of the small x corrections for a discrete number of values of α_s . The first issue is then selecting the value of our α_s grid, nearest to the true one.

The routines I wrote take as input *alphas*, i.e. the true value of α_s . The values of the α_s grid are $N_{\alpha_s} = 57$ and are stored in a vector (AS_GRID) of N_{α_s} components. What we need then is selecting the component of the vector corresponding to the adequate value of α_s . To find it, I use the following algorithm.

1. Compare *alphas* with the lowest and the greatest value of AS_GRID: if it is lower than AS_GRID(1) then AS_GRID(1) is the grid value nearest to *alphas*, if it greater than AS_GRID(57) then the nearest value is AS_GRID(57).
2. If the previous conditions are not satisfied, then we search for the pair of values of the grid, such that

$$\text{AS_GRID}(k) < \textit{alphas} < \text{AS_GRID}(k + 1). \quad (4.7)$$

To choose between the two values one needs to compute the distance between *alphas* and AS_GRID(k) or AS_GRID(k+1) and take the component k_α of AS_GRID for which the distance is lower.

Once the correct component of AS_GRID has been chosen, one has to find the actual expression of the small x resummed correction.

For each quantities of Table 4.1 and for each value of AS_GRID, we have a set of N_c coefficients, which must be replaced in the parametrization's Mellin transform (4.3) or (4.6) to get the actual form of the N space small x resummed correction. Thus now we need to select the right set of coefficients.

Provided that for each quantity of Table 4.1 there is one file containing the N_c

coefficients of the fit for all the value of α_s , first we read all the coefficients for a given quantity and store them in a vector of $57 \cdot N_c$ components. Then, defining

$$m = N_c \cdot (k_\alpha - 1) + 1 \quad \text{and} \quad n = N_c \cdot k_\alpha, \quad (4.8)$$

the components of the coefficients' vector to be selected are the ones between m and n .

In this way the small x resummation is fully implemented within the FastKernel method. In the next section I will show the results of the check I made to understand if the implementation is correct.

4.2.3 Checks and results

To check if the small x resummation is correctly implemented in the Fortran code, we need to verify that the Mellin inversion of the resummed correction to the anomalous dimension, as computed by the FastKernel code, has the same form of the starting interpolations (see Figures 4.1, 4.2, 4.7, 4.8). The Mellin inversion is performed with the Fixed Talbot algorithm [6], which is the same algorithm implemented in the FastKernel code

For the splitting functions, this check gives a positive result. From Figures 4.13, 4.14, 4.15, 4.16, it is evident that the agreement is almost perfect.

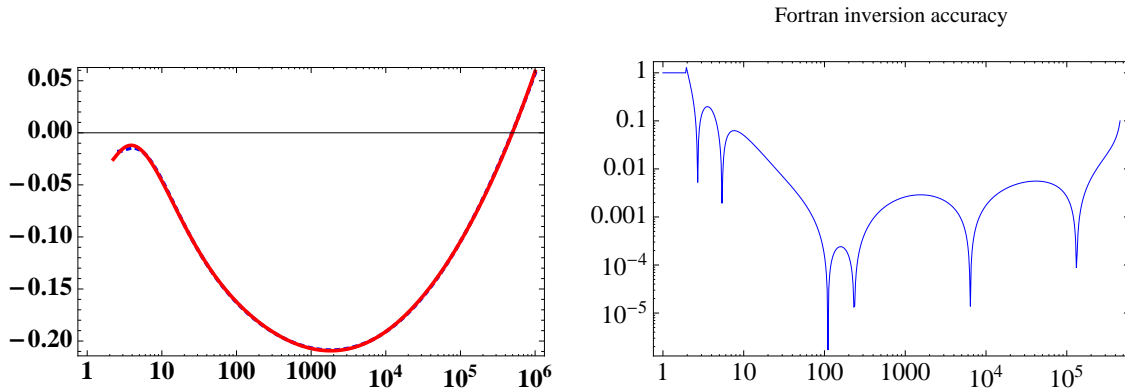


Figure 4.13: Left panel: $\Delta P_{gg}(\text{left})$ for $\alpha_s = 0.2$: original interpolation (red) and result of the Mellin inversion of the resummed correction to the anomalous dimension, as computed by the FastKernel code (red). Right panel: accuracy σ_{rel} of the Mellin inversion.

Also for the coefficient functions we have a very good result, as shown in Figures 4.17, 4.18, 4.19, 4.20. All these checks confirm that the implementation of small x resummed quantities is correct.

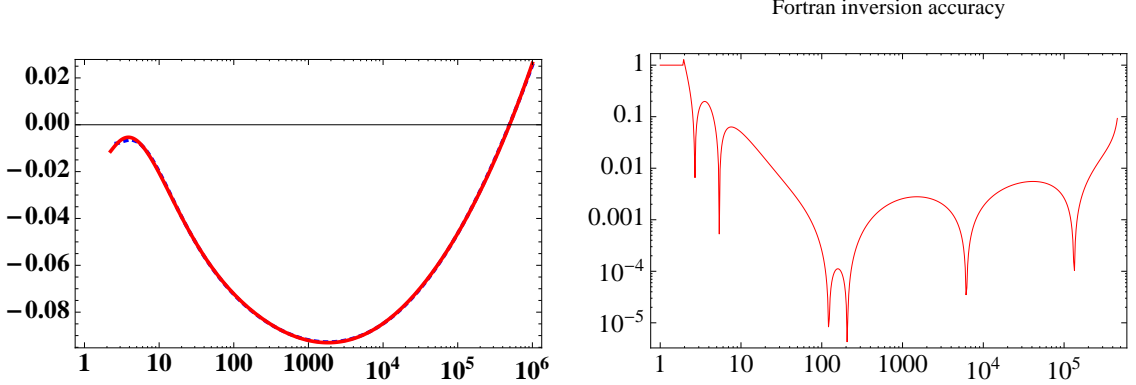


Figure 4.14: Left panel: ΔP_{gg} for $\alpha_s = 0.2$: original interpolation (red) and result of the Mellin inversion of the resummed correction to the anomalous dimension, as computed by the FastKernel code (red). Right panel: accuracy σ_{rel} of the Mellin inversion.

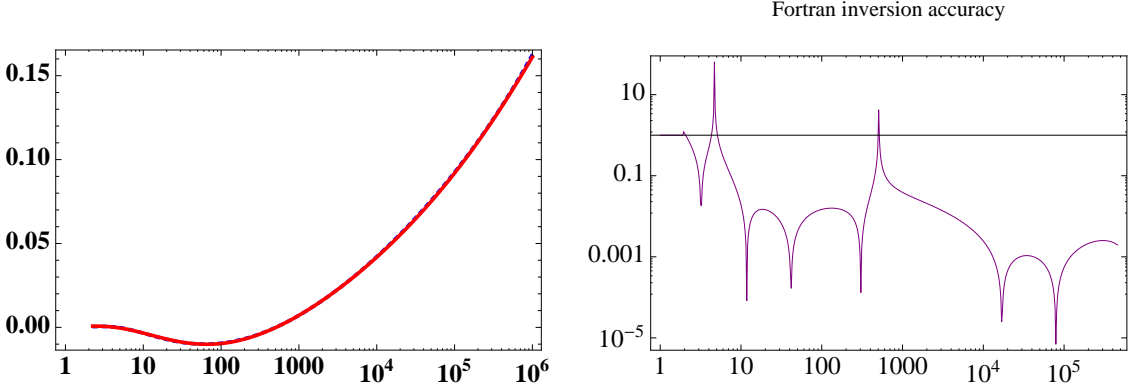


Figure 4.15: Left panel: ΔP_{gg} for $\alpha_s = 0.2$: original interpolation (red) and result of the Mellin inversion of the resummed correction to the anomalous dimension, as computed by the FastKernel code (red). Right panel: accuracy σ_{rel} of the Mellin inversion.

4.3 Future works

Once the small x resummed corrections have been correctly implemented in the FastKernel code, the next step is perform the evolution of PDFs with the new kernels computed at LLx accuracy and compare the results with the analytic results of ABF [1]. After computing the physical observables, one can actually perform a global parton fit and find a set of small x resummed PDFs.

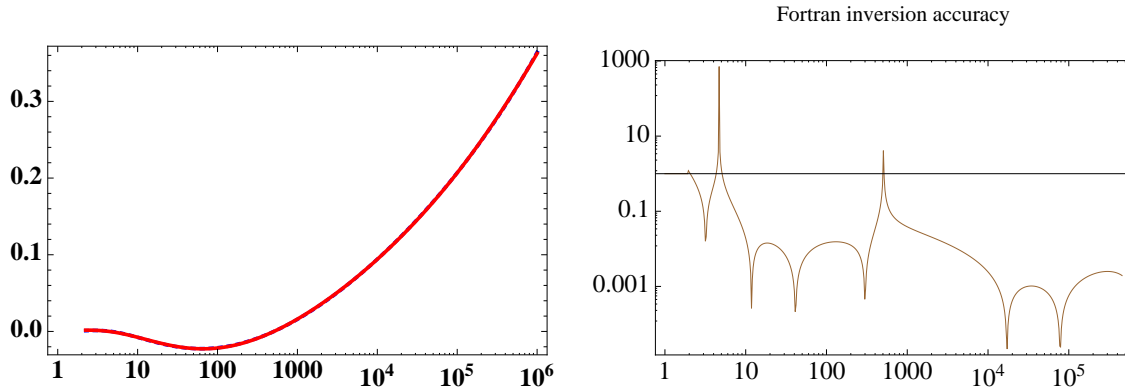


Figure 4.16: Left panel: ΔP_{gg} for $\alpha_s = 0.2$: original interpolation (red) and result of the Mellin inversion of the resummed correction to the anomalous dimension, as computed by the FastKernel code (red). Right panel: accuracy σ_{rel} of the Mellin inversion.

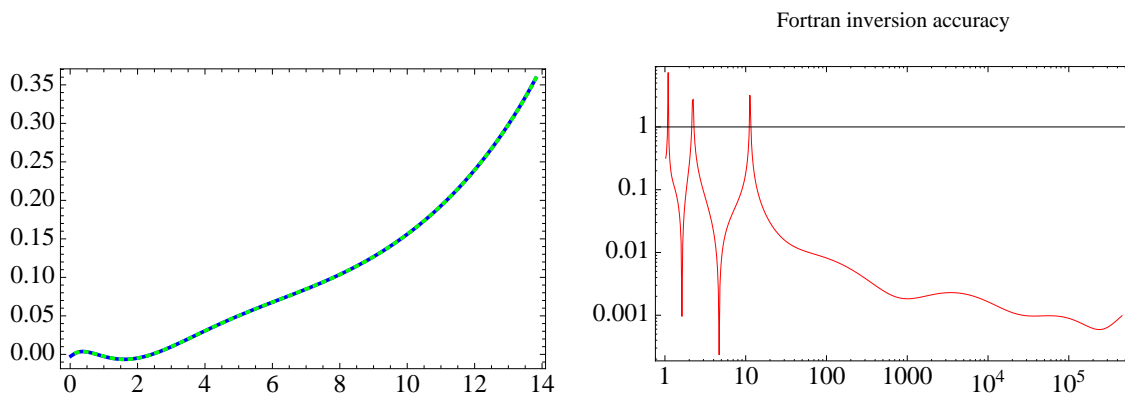


Figure 4.17: Left panel: ΔC_2^g (left) for $\alpha_s = 0.2$: original interpolation (red) and result of the Mellin inversion of the resummed correction to the anomalous dimension, as computed by the FastKernel code (red). Right panel: accuracy σ_{rel} of the Mellin inversion.

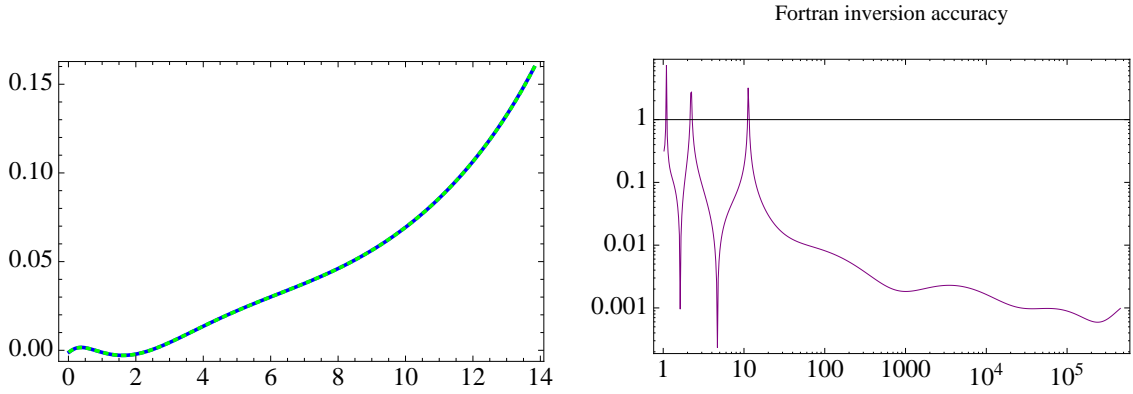


Figure 4.18: Left panel: ΔC_2^g for $\alpha_s = 0.2$: original interpolation (red) and result of the Mellin inversion of the resummed correction to the anomalous dimension, as computed by the FastKernel code (red). Right panel: accuracy σ_{rel} of the Mellin inversion.

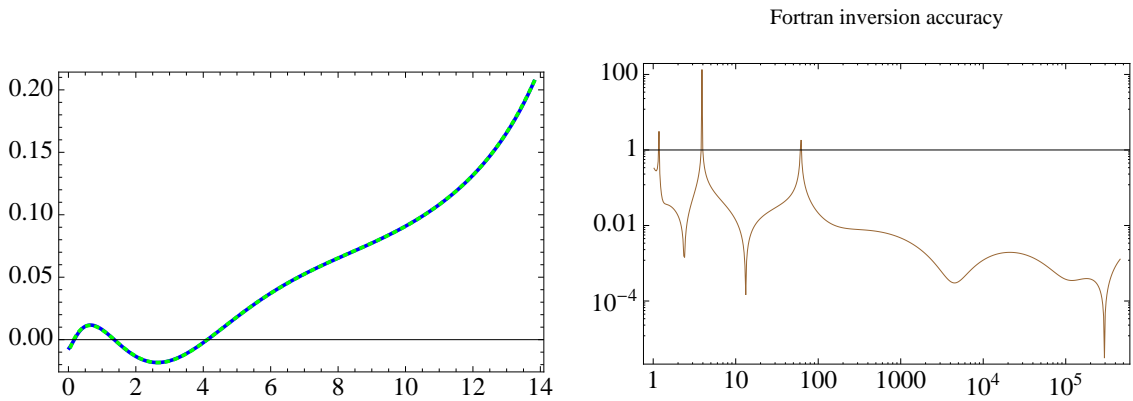


Figure 4.19: Left panel: ΔC_L^g for $\alpha_s = 0.2$: original interpolation (red) and result of the Mellin inversion of the resummed correction to the anomalous dimension, as computed by the FastKernel code (red). Right panel: accuracy σ_{rel} of the Mellin inversion.

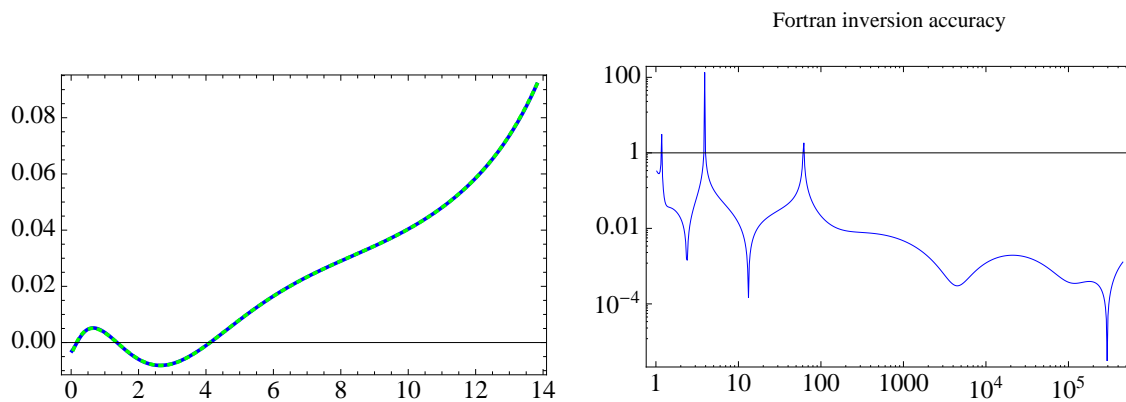


Figure 4.20: Left panel: ΔC_L^q for $\alpha_s = 0.2$: original interpolation (red) and result of the Mellin inversion of the resummed correction to the anomalous dimension, as computed by the FastKernel code (red). Right panel: accuracy σ_{rel} of the Mellin inversion.

Bibliography

- [1] G. Altarelli, R. D. Ball, S. Forte. "Small x resummation with quarks: Deep-Inelastic scattering". *Nucl. Phys.*, B799:199240, 2008.
- [2] NNPDF, R.D. Ball, L. Del Debbio, S. Forte, A. Guffanti, J.I. Latorre, A. Piccione, J. Rojo, M. Ubiali. "A determination of parton distributions with faithful uncertainty estimation". *Nucl. Phys.*, B809:163, 2008.
- [3] NNPDF, R.D. Ball, L. Del Debbio, S. Forte, A. Guffanti, J.I. Latorre, J. Rojo, M. Ubiali. "A first unbiased global NLO determination of parton distributions and their uncertainties". *Nucl. Phys.*, B838:136-206, 2010.
- [4] S. Catani, M. Ciafaloni, and F. Hautmann. "High-energy factorization and small x heavy flavor production". *Nucl. Phys.*, B366:135188, 1991.
- [5] M. Ciafaloni, D. Colferai, G. P. Salam and A. M. Stasto. "Renormalisation group improved small- x Greens function". *Phys. Rev.*, D 68 (2003) 114003.
- [6] J. Abate, P.P. Valkó. "Multi-precision Laplace transform inversion". *Int. J. Numer. Meth. Engng*, 60:979993, 2004.
- [7] R.K. Ellis, W.J. Stirling, B.R. Webber. "QCD and collider physics". Cambridge University Press, 1996.
- [8] M.E. Peskin, D.V. Schroeder, "An introduction to Quantum Field Theory". Addison-Wesley, 1995.